The Astrophysical Journal, 698:1380–1397, 2009 June 20 doi:10.1088/0004-637X/698/2/1380
© 2009. The American Astronomical Society. All rights reserved. Printed in the U.S.A.

BALANCING THE ENERGY BUDGET BETWEEN STAR FORMATION AND ACTIVE GALACTIC NUCLEI IN HIGH-REDSHIFT INFRARED LUMINOUS GALAXIES

E. J. Murphy[1], R.-R. Chary[1], D. M. Alexander[2], M. Dickinson[3], B. Magnelli[4], G. Morrison[5,6], A. Pope[3,7], and H. I. Teplitz[1]

[1] *Spitzer* Science Center, MC 314-6, California Institute of Technology, Pasadena, CA 91125, USA; emurphy@ipac.caltech.edu
[2] Department of Physics, Durham University, Durham DH1 3LE, UK
[3] National Optical Astronomy Observatory, Tucson, AZ 85719, USA
[4] Laboratoire AIM, CEA/DSM-CNRS-Université Paris Diderot, DAPNIA/Service d'Astrophysique, Bât. 709, CEA-Saclay, F-91191 Gif-sur-Yvette Cédex, France
[5] Institute for Astronomy, University of Hawaii, Honolulu, HI 96822, USA
[6] Canada–France–Hawaii Telescope, Kamuela, HI 96743, USA
[7] *Spitzer* Fellow.

Received 2008 December 15; accepted 2009 April 15; published 2009 May 29

ABSTRACT

We present deep *Spitzer* mid-infrared spectroscopy, along with 16, 24, 70, and 850 μm photometry, for 22 galaxies located in the Great Observatories Origins Deep Survey-North (GOODS-N) field. The sample spans a redshift range of $0.6 \lesssim z \lesssim 2.6$, 24 μm flux densities between $\sim$0.2 and 1.2 mJy, and consists of submillimeter galaxies (SMGs), X-ray or optically selected active galactic nuclei (AGNs), and optically faint ($z_{AB} > 25$ mag) sources. We find that infrared (IR; 8–1000 μm) luminosities derived by fitting local spectral energy distributions (SEDs) with 24 μm photometry alone are well matched to those when additional mid-infrared spectroscopic and longer wavelength photometric data are used for galaxies having $z \lesssim 1.4$ and 24 μm-derived IR luminosities typically $\lesssim 3 \times 10^{12} L_{\odot}$. However, for galaxies in the redshift range between $1.4 \lesssim z \lesssim 2.6$, typically having 24-$\mu$m-derived IR luminosities $\gtrsim 3 \times 10^{12} L_{\odot}$, IR luminosities are overestimated by an average factor of $\sim$5 when SED fitting with 24 μm photometry alone. This result arises partly due to the fact that high-redshift galaxies exhibit aromatic feature equivalent widths that are large compared to local galaxies of similar luminosities. Using improved estimates for the IR luminosities of these sources, we investigate whether their infrared emission is found to be in excess relative to that expected based on extinction-corrected UV star formation rates (SFRs), possibly suggesting the presence of an obscured AGN. Through a spectral decomposition of mid-infrared spectroscopic data, we are able to isolate the fraction of IR luminosity arising from an AGN as opposed to star formation activity. This fraction is only able to account for $\sim$30% of the total IR luminosity among the entire sample and $\sim$35% of the "excess" IR emission among these sources, on average, suggesting that AGNs are not the dominant cause of the inferred "mid-infrared excesses" in these systems. Of the sources identified as having mid-infrared excesses, half are accounted for by using proper bolometric corrections while half show the presence of obscured AGNs. This implies sky and space densities for Compton-thick AGNs of $\sim$1600 deg^{-2} and $\sim 1.3 \times 10^{-4}$ Mpc^{-3}, respectively. We also note that IR luminosities derived from SED fitting the mid-infrared *and* 70 μm broadband photometry agree within $\sim$50% to those values estimated using the additional mid-infrared spectroscopic and submillimeter data. An inspection of the far-infrared (FIR)–radio correlation shows no evidence for evolution over this redshift range. However, we find that the SMGs have IR/radio ratios which are a factor of $\sim$3 lower, on average, than what is measured for star-forming galaxies in the local universe.

Key words: galaxies: evolution – infrared: galaxies – radio continuum: galaxies

Online-only material: color figure

1. INTRODUCTION

A reliable estimation of the star formation rates (SFRs), stellar mass, and active galactic nuclei (AGNs) activity at all redshifts is required in order to obtain a comprehensive understanding of galaxy evolution. Various studies have shown that the SFR density increases by a factor of $\sim$5–10 between $z \sim 0$ and $z \sim 1$ and that $\gtrsim$60% of the total SFR density at $z \sim 1$ is obscured by dust (Elbaz et al. 2002; Chary & Elbaz 2001; Le Floc'h et al. 2005; Magnelli et al. 2009). Until now, these results have relied on deep surveys at 15 μm and 24 μm which sample the redshifted mid-infrared spectral energy distribution (SED) of galaxies.

The mid-infrared (5–40 μm) SED is a complex interplay of broad emission features thought to arise from polycyclic aromatic hydrocarbon (PAH) molecules, silicate absorption features at 9.7 and 18 μm, and a mid-infrared continuum from very small grains (Leger & Puget 1984; Allamandola et al. 1985). Mid-infrared luminosities measured near $\sim$8 μm have been found to correlate with the total infrared (IR; 8–1000) luminosities of galaxies in the local universe (Chary & Elbaz 2001; Elbaz et al. 2002), which itself is a measure of a galaxy's SFR. While a correlation is found, there does exist a large amount of scatter (Dale et al. 2005; Smith et al. 2007; Armus et al. 2007) and systematic departures for low-metallicity systems (Engelbracht et al. 2005; Madden et al. 2006). It is therefore uncertain if these empirical relations between mid-infrared and total IR luminosities ($L_{\rm IR}$) for galaxies in the local universe are applicable for galaxies at higher redshifts.

Recently, data from deep far-infrared (FIR) surveys such as the Far-infrared Deep Legacy Survey (FIDEL; P.I.: M. Dickinson) are confirming the same redshift evolution of the SFR density seen in the mid-infrared and do not show any evolution in the SED of infrared luminous galaxies (e.g.,

Magnelli et al. 2009). Furthermore, individual lensed Lyman break galaxies (LBGs) at $z \sim 2.5$ (Siana et al. 2008; Wilson et al. 2008; Gonzalez et al. 2009), seem to show bolometric corrections similar to those of local galaxies. In contrast, Rigby et al. (2008) have provided evidence that the high-redshift lensed mid-infrared-selected galaxies might show a factor of $\sim$2 stronger rest-frame 8 μm emission compared to their total IR luminosities. Part of the contradiction might be due to the intrinsic scatter in the physical properties of the galaxies, particularly the range of dust color temperatures and emissivities seen for galaxies in the local universe (e.g., Dunne et al. 2000). Individual galaxies detected in the FIR or submillimeter at high redshift, for which the comparisons are made, might be sampling the scatter in the ratio rather than the median trend which the empirical galaxy templates follow.

In order to assess the accuracy of mid-infrared derived bolometric luminosities as a tracer of star formation at $z \sim 2$, Daddi et al. (2007a, 2007b) compared mid-infrared (i.e., observed-frame 24 μm) based SFRs to those derived from extinction-corrected UV emission and radio emission. They found a systematic offset, whereby the mid-infrared-derived bolometric luminosities were systematically higher than alternate SFR estimates, especially among the most intrinsically luminous mid-infrared sources. Furthermore, they found that stacking the X-ray data on these "mid-infrared excess" galaxies revealed the presence of a hard X-ray source suggestive of obscured AGN activity. Since mid-infrared wavelengths are sensitive to warm dust continuum emission arising from AGN activity, Daddi et al. (2007b) concluded that these mid-infrared excesses arise from deeply obscured AGNs and report a space density of Compton thick AGNs which is twice that of all X-ray-detected AGNs at $z \sim 2$.

The detection of a source in hard X-rays does not necessarily imply that an AGN is dominating its energetics as is found for submillimeter galaxies (SMGs) which appear to be both star formation driven and commonly detected in the X-rays (Alexander et al. 2005; Pope et al. 2008a). Furthermore, evidence for "mid-infrared excess" relative to extinction-corrected UV luminosities might simply be evidence for optically thick star formation, a phenomenon which is ubiquitous among ultraluminous infrared galaxies (ULIRGs; $L_{\rm IR} \geqslant 10^{12} L_{\odot}$) in the local universe (Buat et al. 2007). Mid-infrared spectroscopy of galaxy samples selected by their mid-infrared flux densities provides a powerful technique to isolate these various selection effects among infrared luminous sources. By decomposing these spectra, into PAH and continuum components, one can get a handle on the relative fraction of power being emitted by AGN activity within such sources relative to the output related to star formation (e.g., Sajina et al. 2007; Pope et al. 2008a).

The Great Origins Observatories Deep Survey-North (GOODS-N; Dickinson et al. 2003) field, due to the wealth of multiwavelength data spanning the ultraviolet to radio wavelengths, is the optimal field in which to undertake such a relatively unbiased survey. Using mid-infrared spectroscopy for 22 sources selected at 24 μm in the GOODS-N field, along with existing 850 μm and additional 70 μm imagery obtained as part of FIDEL, we aim to improve our understanding of the star formation and AGN activity within a diverse group of $0.6 \lesssim z \lesssim 2.6$ galaxies. This is done through a more proper estimate of IR luminosities and the ability to decompose these measurements into star-forming and AGN components.

The paper is organized as follows. In Section 2, we introduce the sample and describe the observations. The determination of IR luminosities from SED fitting, calculation of SFRs, and the decomposition of AGNs and star formation power using the mid-infrared spectroscopy are described in Section 3. The results are presented in Section 4 while their implications are discussed in Section 5. Finally, in Section 6, we summarize our conclusions.

Table 1
Galaxy Positions and Redshifts

ID	R.A. (J2000)	Decl. (J2000)	$z_{\rm opt}$[a]	$z_{\rm IRS}$[a]	$z_{\rm opt}$ Reference
1	12 35 55.13	62 9 1.7	1.875	1.88	1
2	12 36 0.17	62 10 47.3	2.002	2.01	1
3	12 36 3.25	62 11 10.8	0.638	0.63	2
4	12 36 16.11	62 15 13.5	2.578	2.55	1
5	12 36 18.33	62 15 50.4	1.865	2.00	1
6	12 36 19.13	62 10 4.3	...	2.21	...
7	12 36 21.27	62 17 8.1	1.992	1.99	3
8	12 36 22.48	62 15 44.3	0.639	0.64	2
9	12 36 22.66	62 16 29.5	2.466	1.79	1,3
10	12 36 33.22	62 8 34.7	0.934	0.94	2
11	12 36 34.51	62 12 40.9	1.219	1.22	4
12	12 36 37.02	62 8 52.2	...	2.01	...
13	12 36 53.22	62 11 16.7	0.935	0.93	5
14	12 36 55.93	62 8 8.1	0.792	0.79	5
15	12 36 56.47	62 19 37.5	1.362	2.20	6
16	12 37 1.59	62 11 46.2	0.884	1.73	7
17	12 37 4.34	62 14 46.1	2.211	2.21	8
18	12 37 11.37	62 13 31.1	1.996	1.98	3
19	12 37 16.59	62 16 43.2	...	1.82	...
20	12 37 18.27	62 22 58.9	...	1.88	...
21	12 37 26.49	62 20 26.6	...	1.75	...
22	12 37 34.52	62 17 23.2	0.641	0.64	5

Notes.
[a] Optical spectroscopic redshift.
[b] Mid-infrared (IRS) spectroscopic redshift.
(1) Chapman et al. 2005; (2) Wirth et al. 2004; (3) Swinbank et al. 2004; (4) Cohen et al. 1996; (5) Cowie et al. 2004; (6) D. Stern et al. 2009, in preparation; (7) Cohen et al. 2000; (8) Steidel et al. 2002.

2. THE SPECTROSCOPIC SAMPLE AND MULTIWAVELENGTH PHOTOMETRY

The mid-infrared spectroscopic sample presented here consists of 22 sources drawn from 24 μm detections in the GOODS-N (Dickinson et al. 2003) field. Galaxy coordinates and IDs used throughout the text are given in Table 1. The sample was chosen to span a range in redshift from $0.6 \lesssim z \lesssim 2.6$ and contain a variety of object types: SMGs, X-ray or optically selected AGN, typical luminous infrared galaxies (LIRGs; $10^{11} \leqslant L_{\rm IR} < 10^{12} L_{\odot}$), and optically faint (i.e., $z_{\rm AB} > 25$ mag) 24 μm sources. The classification for each object is given in Table 2. To ensure high signal-to-noise ratio (S/N) in the IRS spectra, a flux density cut of $f_{\nu}(24\ \mu{\rm m}) > 200\ \mu$Jy was made, although the median flux density of the sample is 510 μJy. The multiwavelength photometry is given in Table 3.

2.1. IRS Spectroscopy

Spitzer IRS observations were taken as part of *Spitzer* program GO-20456 (P.I.: R.-R. Chary) in 2006 April/May. These low-resolution ($R = \lambda/\Delta\lambda \sim 100$) spectroscopic observations were made using the spectral staring mode, which observed each target at two nod positions (per cycle) within the slit. In Table 2, we provide the ramp times and the total number of cycles used

Table 2
Spitzer IRS Observations Summary

ID	Number of Cycles per Module[a] SL1 (240 s)[b]	LL1 (120 s)[b]	LL2 (120 s)[b]	Selection Criteria[c]
1	···	40	31	OF, X-ray, SMG
2	···	10	6	SMG
3	10	···	6	X-ray, LIRG
4	···	70	···	OF, X-ray, SMG
5	···	55	35	OF, SMG
6	···	55	···	OF, SMG
7	···	45	35	OF, SMG
8	15	···	12	X-ray, LIRG
9	···	45	···	X-ray, SMG
10	10	···	12	X-ray
11	15	···	20	X-ray, SMG
12	···	40	31	OF
13	···	···	35	SMG
14	12	···	8	X-ray, LIRG
15	···	16	12	OF
16	20	···	12	OF, X-ray, SMG
17	···	45	···	NL-AGN
18	···	28	20	X-ray, SMG
19	···	28	20	OF, X-ray
20	···	29	20	OF
21	···	10	6	X-ray
22	10	···	12	LIRG

Notes.
[a] Observations were made using the IRS staring mode which observes each target at two nod positions per cycle.
[b] Ramp times per cycle.
[c] Selection criteria: OF, optically faint; X-ray, X-ray detected; SMG, submillimeter galaxy (included in Pope et al. 2008a); LIRG, typical LIRG; NL-AGN, narrow-line AGN.

per low-resolution module. We note that a study focusing on the SMGs included in this sample can be found in Pope et al. (2008a) where complete details on the observation strategy and data reduction steps are also presented. The actual spectra, shifted into the rest frame, are shown in Figure 1 along with associated errors. The expected positions of the 3.3, 6.2, 7.7, 8.6 and 11.3 μm PAH features, along with the 9.7 μm silicate absorption feature, are indicated with vertical lines.

For cases where PAH features in the IRS spectra are clearly identified, redshifts were measured directly as described in Pope et al. (2008a). The redshifts for the remaining galaxies were taken from existing optical spectroscopy (Table 1). We note that there were some discrepancies in the IRS and optical spectroscopic redshifts (i.e., GN-IRS 5,9,15, and 16) in which case the IRS-derived redshifts were used. GN-IRS 5 and 9 are both SMGs for which the discrepancies between their IRS and optical redshifts are discussed in Appendix B of Pope et al. (2008a). Pope et al. (2006) report that the optical ($z = 0.884$) redshift associated with GN-IRS 16, also an SMG, is not the true counterpart. The discrepancy for GN-IRS 15 is thought to arise from a superposition of sources. The optical morphology of this source is quite complex, having several components and a range of colors. Thus, we strongly suspect that we are seeing a superposition of a mid-infrared bright galaxy located at $z = 2.20$ and a foreground galaxy at $z = 1.362$.

The final redshift range among the sample spans $0.6 \lesssim z \lesssim 2.6$ with a median of 1.88. A total of 15 galaxies have a redshift between $1.4 \lesssim z \lesssim 2.6$, which is almost exactly the nominal redshift range for the BzK color selection where a comparison with the Daddi et al. (2007b) results are appropriate. In addition, seven of the galaxies have redshifts between $0.6 \lesssim z \lesssim 1.2$ and are intended to be representative of the LIRG population.

2.2. *Mid- and Far-Infrared* Spitzer *Imaging*

Infrared imaging of the GOODS-N field was obtained at 16, 24, and 70 μm using the *Spitzer Space Telescope*. The 24 μm observations of GOODS-N were taken as part of the GOODS legacy program (P.I.: Dickinson) and reach an rms of $\sim$5 μJy (see Chary 2007). The spectroscopic sample presented here spans the range 220–1220 μJy.

IRS peak-up observations at 16 μm (Teplitz et al. 2005) were made covering an area slightly less extended than the GOODS-N 24 μm map. Only one of the sample galaxies, GN-IRS 1, lies outside the areal coverage of the 16 μm map. These 16 μm data have an rms of $\sim$6 μJy and only sources with a S/N greater than 5 were considered as a detection. Of the 21 sources in the 16 μm image field of view, two were not detected and their flux densities were set to the upper limit value of 30 μJy. The 16 μm flux densities among the detected sources span a factor of $\sim$25, ranging from $\sim$40 to 1050 μJy with a median value of $\sim$280 μJy.

MIPS 70 μm observations were carried out as part of program GO-3325 (P.I.: Frayer) and the FIDEL project (P.I.: Dickinson). The full field extends beyond the 24 μm coverage and data processing details can be found in Frayer et al. (2006). The typical point-source noise of the 70 μm data is $\sim$0.55 mJy (Frayer et al. 2006), $\sim$1.6 times larger than the confusion noise level of $\sigma_c = 0.35 \pm 0.15$ mJy estimated by Frayer et al. (2009). Sources having a flux density >2 mJy and a S/N > 6 were considered detections, leading to a total of nine sources; all other sources were assigned an upper limit of 3 mJy since this value corresponds to a differential completeness of $\sim$80% (Magnelli et al. 2009). The median 70 μm flux density among the detected sources is $\sim$5.5 mJy and ranges between $\sim$2.2 and 14.2 mJy, spanning a factor of roughly 6. The photometric uncertainty including calibration uncertainties and confusion is $\sim$10% at 16 and 24 μm and $\sim$20% at 70 μm.

2.3. *X-ray Imaging*

X-ray imaging of GOODS-N was obtained with the *Chandra* X-ray Observatory for a 2 Ms exposure (Alexander et al. 2003). The full band (0.5–8.0 keV) and hard band (2.0–8.0 keV) on-axis sensitivities are $\sim 7.1 \times 10^{-17}$ and 1.4×10^{-16} erg cm^{-2} s^{-1}, respectively. Of the 22 sample galaxies, 12 were matched with an X-ray counterpart reported by Alexander et al. (2003). For the remaining 10 sources, upper limits were measured assuming $\Gamma = 1.4$.

Among the 12 X-ray detected sources we find that the 0.5–8.0 keV flux spans more than 2 orders of magnitude, ranging from 9 to 1120×10^{-17} erg cm^{-2} s^{-1}, with a median flux of 56×10^{-17} erg cm^{-2} s^{-1} (Table 3). Eight sources have secure detections in the hard band (2.0–8.0 keV) while only upper limits could be measured for the remaining 14 sources. Of those sources detected, the range in the 2.0–8.0 keV flux spans between 25 and 1050×10^{-17} erg cm^{-2} s^{-1} (i.e., a factor of $\sim$40) with a median flux of $\sim 100 \times 10^{-17}$ erg cm^{-2} s^{-1}.

2.4. *Optical Imaging*

The GOODS-N field has been imaged extensively in four bands, B_{435}, V_{606}, i_{775}, and z_{850} using the Advanced Camera for Surveys (ACS) on the *Hubble Space Telescope* (Giavalisco et al.

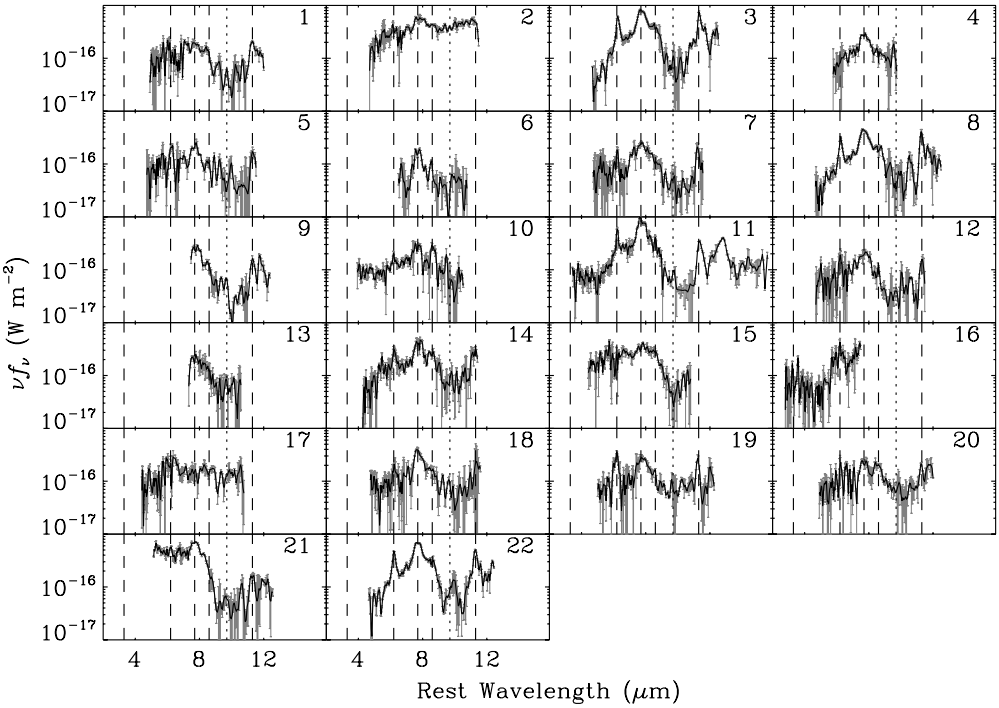

Figure 1. Mid-infrared IRS spectra for each of the 22 sample galaxies. Each spectra is shown with associated errors in the rest-frame and has been smoothed to the instrument resolution. The expected positions of the 3.3, 6.2, 7.7, 8.6, and 11.3 μm PAH features are indicated by *dashed* vertical lines; the expected position of the 9.7 μm silicate absorption feature is indicated with a dotted vertical line.

2004). Additional ground-based imaging of GOODS-N in the *U* band was obtained using the prime-focus MOSAIC camera on the KPNO Mayall 4 m telescope (Giavalisco et al. 2004; Capak et al. 2004). The 3σ upper limits of the *UBViz* photometry are 0.027, 0.048, 0.048, 0.091, and 0.131 μJy, respectively.

2.5. Radio Continuum Imaging

The GOODS-N field was observed with the Very Large Array (VLA) for a total of 165 hr using all four configurations (G. Morrison et al. 2009, in preparation). Given that the VLA is a centrally condensed array, the observing time per configuration was scaled as follows, A-array (1), B-array (1/4), C-array (1/16), and D-array (1/64) (Owen & Morrison 2008). This integration time scaling provides the best sensitivity for larger sources. The final radio map has a local rms at the phase center of $\sim$4 μJy. All sources in the IRS spectroscopic sample were matched with a S/N $>$ 4 radio source to a radius of 1$''$ except for GN-IRS 13, which had a S/N $\sim$ 3.3. The 20 cm flux densities span a factor of $\sim$9 (i.e., $\sim$21–202 μJy) with a median value of $\sim$98 μJy.

2.6. Submillimeter Imaging

The GOODS-N field was imaged at 850 μm by a number of programs using the Submillimeter Common-User Bolometer Array (SCUBA) and the data were combined into the SCUBA "supermap" (Borys et al. 2003; Pope et al. 2005). The eight SMGs targeted for IRS spectroscopy were selected from the "supermap" sources with robust identifications (Pope et al. 2006) in addition to three SCUBA photometry sources from Chapman et al. (2005). Only two of the 11 SMGs are detected at 70 μm (Huynh et al. 2007). The 850 μm flux densities span a range between 2 and 9 mJy with a median flux density 5.2 mJy. For the remaining nondetected IRS targets, 3σ upper limits were calculated from the 850 μm SCUBA supermap. The only exception is GN-IRS 20 which lies outside the areal coverage of the SCUBA maps.

3. DATA ANALYSIS

In the following section we describe our methods for calculating infrared (IR; 8–1000 μm) luminosities ($L_{\rm IR}$) for each of the sample galaxies along with IR and UV (1500 Å) based SFRs. For all calculations we assume a Hubble constant of 71 km s^{-1}, and a standard lambda cold dark matter (ΛCDM) cosmology with $\Omega_{\rm M} = 0.27$ and $\Omega_\Lambda = 0.73$. Due to the small number of sample galaxies, all average properties of the sample are given as a median rather than taking a mean.

3.1. Determining Infrared Luminosities from SED Fitting

Infrared luminosities are extrapolated by fitting the mid-infrared spectra and photometric data to the SED templates of Chary & Elbaz (2001), and then integrating between 8 and 1000 μm. We choose to fit to the templates of Chary & Elbaz (2001) since they have been found to exhibit 24/70 μm flux density ratios which are more representative of the average actually measured for galaxies at $z \sim 1$ than either the Dale & Helou (2002) or Lagache et al. (2003) templates (Magnelli et al. 2009). The best-fit SEDs are determined by a χ^2 minimization procedure in which the SED templates are allowed to scale such that they are being fitted for luminosity and temperature separately. Consequently, the amplitude and shape of the SEDs scale independently to best match the observations. Weights are derived using the uncertainties of the input photometry (i.e., the S/N of each input photometric band). When fitting the mid-infrared spectra, having *N* individual measurements for each wavelength in the spectra, the individual flux density is weighted by its S/N and an additional factor of $1/N$ so as to not give too much weight to the mid-infrared portion of the spectrum in the fitting. The normalization constant is then

Table 3
Multiwavelength Photometry

ID	$f_{0.5-8.0\,\mathrm{keV}}/10^{-17}$ (erg cm^{-2} s^{-1})	$f_{2.0-8.0\,\mathrm{keV}}/10^{-17}$ (erg cm^{-2} s^{-1})	Γ^{a}	$f_\nu(B)$ (μJy)	$f_\nu(V)$ (μJy)	$f_\nu(i)$ (μJy)	$f_\nu(z)$ (μJy)	$f_\nu(16\,\mu\mathrm{m})$ (μJy)	$f_\nu(24\,\mu\mathrm{m})$ (μJy)	$f_\nu(70\,\mu\mathrm{m})$ (μJy)	$f_\nu(850\,\mu\mathrm{m})$ (μJy)	$S_\nu(20\,\mathrm{cm})$ (μJy)
1	1120.0	1050.0	0.44	<0.027	<0.048	<0.048	<0.13	...	374	<3000	5400	201.89
2	<19.9	<34.1	1.40[b]	0.032	0.212	0.353	0.71	496.8	1220	4030	7900	127.46
3	41.0	<32.1	1.45[c]	2.572	3.993	11.941	35.84	774.7	1210	11100	<24200	153.07
4	102.0	79.7	0.97	<0.027	<0.048	0.072	0.19	60.2	303	<3000	4900	34.33
5	<14.0	<21.4	1.40[b]	<0.027	<0.048	<0.048	<0.13	42.1	330	<3000	7500	171.46
6	<14.4	<23.9	1.40[b]	<0.027	<0.048	<0.048	<0.13	<30.0	215	<3000	5200	21.72
7	<10.9	<17.4	1.40[b]	<0.027	<0.048	<0.048	<0.13	<30.0	347	<3000	8900	169.35
8	32.1	25.4	1.06	3.661	5.328	12.198	30.46	399.7	721	11100	<3500	38.94
9	102.0	114.0	−0.50[c]	0.167	0.315	0.355	0.72	113.3	414	<3000	7700	95.91
10	515.0	255.0	2.01	<0.027	3.258	5.515	13.29	555.8	773	4460	<6500	42.69
11	28.9	<17.4	1.63[c]	0.752	1.073	1.442	6.33	993.6	446	13200	2200	202.10
12	<15.7	<26.6	1.40[b]	0.091	0.125	0.189	0.36	58.8	367	<3000	<6100	81.82
13	<9.2	<14.4	1.40[b]	0.866	1.274	2.707	11.35	302.7	367	<3000	2100	37.88
14	24.7	<27.3	1.35[c]	0.188	0.306	2.088	13.57	593.9	832	14200	<10600	125.16
15	<19.5	<35.3	1.40[b]	<0.027	0.061	0.081	0.22	283.6	714	2210	<9500	42.68
16	9.0	<12.2	1.40	<0.027	<0.048	0.063	0.27	217.0	710	<3000	3900	107.85
17	<12.8	<22.6	1.40[b]	0.700	0.607	0.554	0.84	222.7	376	<3000	<12000	28.33
18	55.5	52.1	0.62	<0.027	0.321	0.654	1.70	99.6	537	<3000	5200	127.64
19	42.3	40.7	0.51	<0.027	<0.048	<0.048	<0.13	174.6	512	<3000	<13900	83.43
20	<49.4	<87.8	1.40[b]	<0.027	<0.048	0.127	0.36	115.5	498	<3000	...	33.09
21	140.0	132.0	0.48	0.032	<0.048	0.171	0.57	1050.7	932	3440	<6200	98.16
22	<21.5	<34.3	1.40[b]	0.540	1.019	5.008	24.32	580.6	750	5530	<18200	121.83

Note.
[a] Photon index: [b] indicates the assumed index used when only upper limits were measured; [c] indicates that the given photon index is an upper or lower limit.

determined by a weighted sum of observed-to-template flux density ratios for all input data used in the fitting. Errors in the fits are determined by a standard Monte Carlo approach using the photometric uncertainties of the input flux densities.

Since we are interested to see to what extent the mid-infrared excesses reported by Daddi et al. (2007a, 2007b) can be solely attributed to improper SED fitting rather than the presence of an embedded AGN, we compute IR luminosities in a number of ways. First, like Daddi et al. (2007a), we perform the SED fitting using the 24 μm flux density alone; Chary & Elbaz (2001) and Dale et al. (2001) SED templates are fit independently, and their integrated 8–1000 μm luminosities are then averaged. The associated IR luminosity is designated as L_{IR}^{24}. The difference between the resultant L_{IR}^{24} from the two sets of SED templates is characterized as a systematic error. We emphasize here that IR luminosities derived in this manner assume that the mid-infrared to total-infrared correlations imprinted in local SED templates are valid at all redshifts.

Next, we use all available spectroscopic and photometric data in the SED fitting: IRS spectra, 16, 24, 70, and 850 μm flux densities where possible. IR luminosities for four out of the 22 sources that are neither detected at 70 or 850 μm (i.e., GN-IRS 12, 17, 19, and 20) are estimated by averaging the IR luminosities from the best-fit Chary & Elbaz (2001) and Dale et al. (2001) SEDs. Due to the nondetection of the four sources at wavelengths close to the peak of the FIR emission, these IR luminosities are considered to be upper limits. In the cases where only upper limit values are available for the photometric data, they are not incorporated into the χ^2 minimization but are used to reject fits which have flux densities above the associated upper limit. The IR luminosities derived from these fits are labeled as $L_{\mathrm{IR}}^{\mathrm{all}}$ and are assumed to be the best-fit estimate of the true IR luminosity for each source. In addition, we also calculate IR luminosities by fitting the SED templates to all available photometry (i.e., including the 850 μm data where possible) to assess how well the PAH features can be characterized by fitting photometric data alone. These values are labeled as $L_{\mathrm{IR}}^{\mathrm{phot}}$. We give L_{IR}^{24}, $L_{\mathrm{IR}}^{\mathrm{all}}$, and $L_{\mathrm{IR}}^{\mathrm{phot}}$ values for each galaxy in Table 4.

Since it is more likely that mid-infrared spectroscopy and submillimeter imaging will not be available for a large number of sources in many deep fields, we also calculate IR luminosities as above excluding these data. A comparison of these IR luminosities, identified as $L_{\mathrm{IR}}^{16,24,70}$, to those calculated using all available photometry will help quantify the reliability of SED fitting using 16–70 μm photometry alone. The IR luminosities derived by this fitting method are also given in Table 4 and are considered to be upper limits for sources not detected at 70 μm.

To illustrate the differences in the best-fitting SEDs using these four methods, we plot the best-fitting Chary & Elbaz (2001) templates along with the spectroscopic and photometric data, for three different sources (GN-IRS 2, 4, and 15) in Figure 2. A comparison of each fitting method zoomed in on the mid-infrared range of 5–15 μm, where PAH emission may be present, is also shown for each galaxy in Figure 3 along with the actual spectra. While the SMGs in our sample have been presented in Pope et al. (2008a), we note that our SED fitting method differs from theirs. We do not include an extinction term and exclude the radio photometry which allows us to assess the FIR–radio correlation among the galaxies. Consequently, for the SMGs in our sample we find that the Pope et al. (2008a) luminosities range from being a factor of ∼0.8 to ∼4.6 times

Table 4
Infrared Luminosities and Associated Parameters

ID	$\log L_{\rm IR}^{24}$ ($L_\odot$)	$\log L_{\rm IR}^{16,24,70}$ ($L_\odot$)	$\log L_{\rm IR}^{\rm phot}$ ($L_\odot$)	$\log L_{\rm IR}^{\rm all}$ ($L_\odot$)	$\log L_{\rm IR}^{\rm RC}$ ($L_\odot$)	$\log L_{\rm AGN}$ ($L_\odot$)	mid-IR AGN Fraction (%)	$q_{\rm IR}$
(1)	(2)	(3)	(4)	(5)	(6)	(7)	(8)	(9)
1	12.79	<12.46	12.12	12.12	13.25	11.89	0.50	1.51
2	13.62	12.90	12.90	13.04	13.12	12.69	0.79	2.56
3	11.85	11.79	11.79	11.78	12.00	<11.04	<0.25	2.42
4	13.49	<13.00	12.48	12.83	12.79	12.21	0.49	2.69
5	12.86	<12.44	12.73	12.73	13.25	11.86	0.46	2.13
6	12.84	<12.60	12.73	12.71	12.45	<11.78	<0.48	2.90
7	12.87	<12.29	12.21	12.21	13.23	11.43	0.18	1.62
8	11.64	11.64	11.64	11.59	11.41	<10.77	<0.23	2.82
9	12.77	<12.54	12.09	12.09	12.88	11.63	0.30	1.86
10	12.03	11.86	11.86	11.89	11.86	11.35	0.44	2.67
11	12.28	12.39	12.38	12.38	12.81	<11.63	<0.36	2.22
12	12.93	<12.48	<12.48	<12.33	12.93	<11.83	<0.52	2.05
13	11.66	<11.50	11.49	11.50	11.80	<11.34	<0.51	2.35
14	11.90	11.91	11.91	11.91	12.15	10.99	0.22	2.41
15	13.55	12.78	12.78	12.76	12.74	12.44	0.69	2.66
16	13.07	<12.53	12.39	12.39	12.90	<11.93	<0.51	2.14
17	13.19	<12.51	<12.51	<12.74	12.56	12.42	0.95	2.82
18	13.13	<12.54	12.35	12.35	13.11	<11.80	<0.33	1.89
19	12.94	<12.23	<12.24	<12.23	12.84	11.69	0.29	2.04
20	12.97	<12.47	<12.47	<12.29	12.47	11.86	0.41	2.47
21	13.23	12.65	12.65	12.65	12.87	12.40	0.62	2.43
22	11.66	11.60	11.60	11.60	11.92	<11.04	<0.29	2.32

Notes. Column (1): source ID. Column (2): 24-μm-derived IR luminosity. Column (3): IR luminosity derived from SED fitting photometric *Spitzer* data: 16, 24, and 70 μm photometry where available. Column (4): IR luminosity derived from SED fitting all photometric data: 16, 24, 70, and 850 μm photometry where available. Column (5): best-fit IR luminosities derived by SED fitting all available data: IRS spectroscopy, 16, 24, 70, and 850 μm photometry where available. Column (6): IR luminosity derived using *K*-corrected 20 cm flux densities and the FIR–radio correlation (see Section 3.2). Column (7): the AGN contribution to the total IR luminosity derived using a mid-infrared spectral decomposition of the IRS data (see Section 3.5). Column (8): the mid-infrared AGN fractions (see Section 3.5). Column (9): the logarithmic IR/radio ratio using the usual q-based parameterization given in Equation (1).

that of our derived IR luminosities, and are a factor of ∼1.2 times larger, on average.

3.2. Infrared Luminosities from the Radio

In the local universe, there exists a remarkably tight correlation between the FIR (42.5–122.5 μm) and predominantly nonthermal radio continuum emission from star-forming galaxies (de Jong et al. 1985; Helou et al. 1985; Condon et al. 1991; Yun et al. 2001). Following a similar quantitative treatment of the FIR–radio correlation (i.e., Helou et al. 1985), we use the total IR (8–1000 μm) luminosity, rather than the FIR fraction, to parameterize the IR–radio correlation such that,

$$q_{\rm IR} \equiv \log\left(\frac{L_{\rm IR}}{3.75\times10^{12}L_\nu(20\ {\rm cm})}\right). \quad (1)$$

For a sample of 164 galaxies without signs of AGN activity, Bell (2003) reports a median $q_{\rm IR}$ value of 2.64 and a scatter of 0.26 dex.

We can estimate the rest-frame 1.4 GHz radio luminosities of our spectroscopic sample using

$$L_\nu(20\ {\rm cm}) = 4\pi D_{\rm L}^2 S_\nu(20\ {\rm cm})(1+z)^{\alpha-1}, \quad (2)$$

where $D_{\rm L}$ is the luminosity distance. This calculation includes a bandwidth compression term of $(1+z)^{-1}$ and a *K*-correction of $(1+z)^{\alpha}$ to rest frame 1.4 GHz. This assumes a synchrotron power law of the form $S_\nu \propto \nu^{-\alpha}$ where the spectral index $\alpha \sim 0.8$ (Condon 1992).

Thus, by setting $\langle q_{\rm IR}\rangle \approx 2.64$, we can derive the infrared luminosities from the radio-specific luminosities with

$$L_{\rm IR}^{\rm RC} = 1.64\times10^{15}L_\nu(20\ {\rm cm}). \quad (3)$$

We assign a factor of ∼2 uncertainty to these luminosities since this is the intrinsic scatter among and within (e.g., Murphy et al. 2006, 2008) star-forming systems in the local universe. The radio-based IR luminosities and $q_{\rm IR}$ ratios are given in Table 4 for each galaxy.

3.3. Estimating Star Formation Rates

3.3.1. IR-based SFRs

Using the conversion given in Kennicutt (1998), calibrated for a Salpeter (1955) initial mass function (IMF) with mass limits between 0.1 and 100 $M_\odot$, we can express our IR luminosities as SFRs such that

$$\left(\frac{{\rm SFR_{IR}}}{M_\odot\ {\rm yr}^{-1}}\right) = 1.73\times10^{-10}\left(\frac{L_{\rm IR}}{L_\odot}\right). \quad (4)$$

Since we have estimated IR luminosities in different manners, we identify each corresponding SFR accordingly; $\rm SFR_{IR}^{24}$: SEDs fit by 24 μm flux densities alone; $\rm SFR_{IR}^{all}$: SEDs fit using all available data (i.e., our best-fit estimates); $\rm SFR_{IR}^{RC}$: using the IR–radio correlation to derive corresponding IR luminosities for which to estimate a SFR.

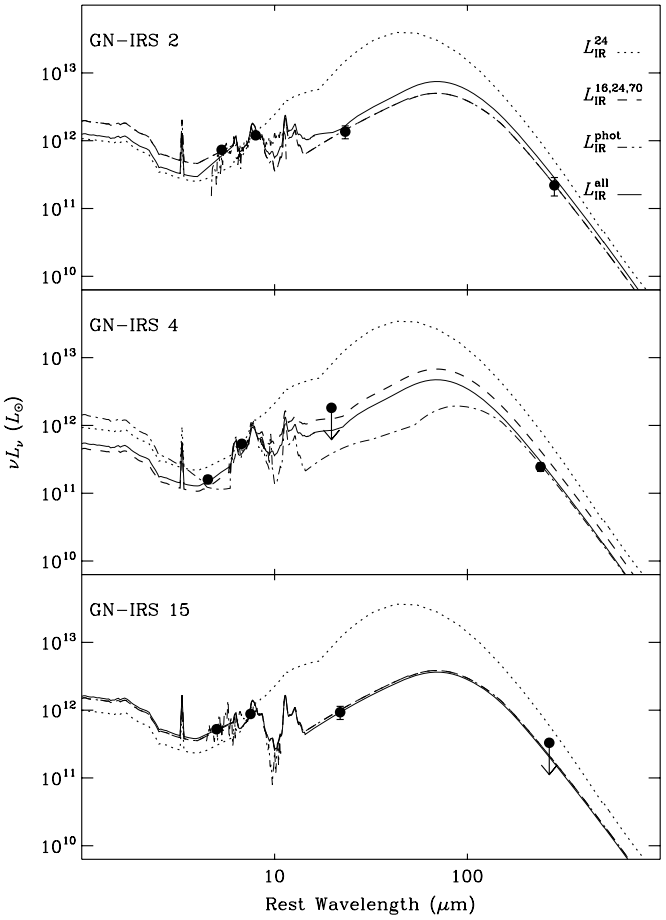

Figure 2. Best-fit SEDs of Chary & Elbaz (2001) for GN-IRS 2 (top panel), 4 (middle panel), and 15 (bottom panel) using only 24 μm flux densities (*dotted* lines), all three *Spitzer* (16, 24, and 70 μm) flux densities (dashed lines), all *Spitzer* and 850 μm photometry (dot-dashed lines), and all *Spitzer* photometry along with the IRS spectra and the 850 μm flux densities (solid lines). The best-fit SEDs associated with $L_{IR}^{16,24,70}$, L_{IR}^{phot}, and L_{IR}^{all} for GN-IRS 15 are very similar, which is why the dashed and dot-dashed lines overlay each other.

3.3.2. UV-Based SFRs

We also estimate SFRs using rest-frame UV-specific luminosities of each galaxy where possible. After putting the observed $UBViz$ data into the rest-frame, 1500 Å flux densities were computed by linearly interpolating along the power-law fits between photometric data points landing in the wavelength range between 1250–2600 Å. Again taking the Kennicutt (1998) conversion, assuming the same Salpeter (1955) IMF ($0.1 - 100 M_\odot$), we can express the resultant UV-specific luminosities in terms of a SFR such that,

$$\left(\frac{\mathrm{SFR_{UV}}}{M_\odot \mathrm{yr}^{-1}}\right) = 5.36 \times 10^5 \left(\frac{L_{\mathrm{UV}}}{L_\odot \mathrm{Hz}^{-1}}\right). \quad (5)$$

For a total of 11 galaxies (i.e., half of the sample) there are less than two photometric points in the rest-frame wavelength range of 1250–2600 Å. In these cases the flux upper limits were used to set a corresponding upper limit on each source's rest-frame UV luminosity.

To estimate the amount of extinction at 1500 Å we use the method described by Meurer et al. (1999) which relates the amount of extinction to the slope of the UV continuum between 1250 and 2600 Å, defined as β. Since the redshifts of the sample galaxies are all less than $z \sim 2.6$, any correction to the UV slope due to absorption by the intergalactic medium is negligible.

While the relation of Meurer et al. (1999) is calibrated for A_{1600}, we use modeled extinction curves (i.e., Weingartner & Draine 2001; Draine 2003), to translate this into an extinction at 1500 Å such that $A_{1500} = 1.05 A_{1600}$ leading to a final relation of

$$A_{1500} = 4.65 + 2.09\beta. \quad (6)$$

We designate SFRs estimated using the extinction-corrected UV luminosities as $\mathrm{SFR_{UV}^{corr}}$. Of the 11 sources having less than two photometric detections in the rest-frame wavelength range of 1250–2600 Å, two (GN IRS 16 and 20) have at least one detection and one reliable upper limit in this wavelength range allowing us to estimate a reasonable lower limit for β. For the remaining nine galaxies, a UV extinction correction was not applied (i.e., $\beta \approx -2.2$). The observed and extinction-corrected UV-specific luminosities are given, along with the values of β, in Table 5.

For the 11 sources which do not have a sufficient number of photometric points in the 1250–2600 Å range to properly measure β, the SFR is considered to be a lower limit given that the extinction correction could not be measured and is likely significant for these sources; i.e., due to the fact that the sample is 24 μm selected, the optical nondetections are probably not from the source being intrinsically dim, but rather from the extinction factor being extremely large.

3.4. X-ray Luminosities

To compare IR and X-ray energetics of these systems, the rest-frame 0.5–8.0 keV and 2.0–8.0 X-ray luminosities are calculated as

$$L_{\mathrm{X}} = 4\pi D_{\mathrm{L}}^2 f_{\mathrm{X}} (1+z)^{\Gamma-2}, \quad (7)$$

where D_{L} is the luminosity distance, f_{X} is the X-ray flux in a particular band, and Γ is the observed or assumed photon index (Table 3). The 0.5–8.0 and 2.0–8.0 keV luminosities are given in Table 5. We also note here that three of the 12 X-ray sources (i.e., 25%) are optically faint, having only IRS-derived redshifts between $1.7 \lesssim z \lesssim 1.9$. This is precisely the redshift range where optically faint X-ray sources are predicted to lie (Alexander et al. 2001; Mainieri et al. 2005).

3.5. Estimating AGN Contributions

Using the IRS data, we follow the procedure described in detail by Pope et al. (2008a) to quantify the AGN contribution to the total IR energy budget. This is done by first decomposing the IRS spectra into two components; one associated with star formation (PAH template) and the other associated with the hot dust continuum emission arising from an embedded AGN. The star-forming component is fit using the starburst composite template of Brandl et al. (2006) while the AGN component is characterized by a power law with both normalization and slope as free parameters. The effect of extinction is considered independently for the PAH and continuum components using a modeled extinction curve (i.e., Weingartner & Draine 2001; Draine 2003). Upon finding the best fit between the spectra and combination of PAH template plus continuum component, the fraction of mid-infrared emission arising from the continuum component is taken to be the AGN contribution. For those galaxies whose spectra did not have high enough S/N or lacked PAH features to allow for a proper decomposition, an upper limit to the AGN strength was obtained by fitting a power law to the continuum of the spectra and integrating below it.

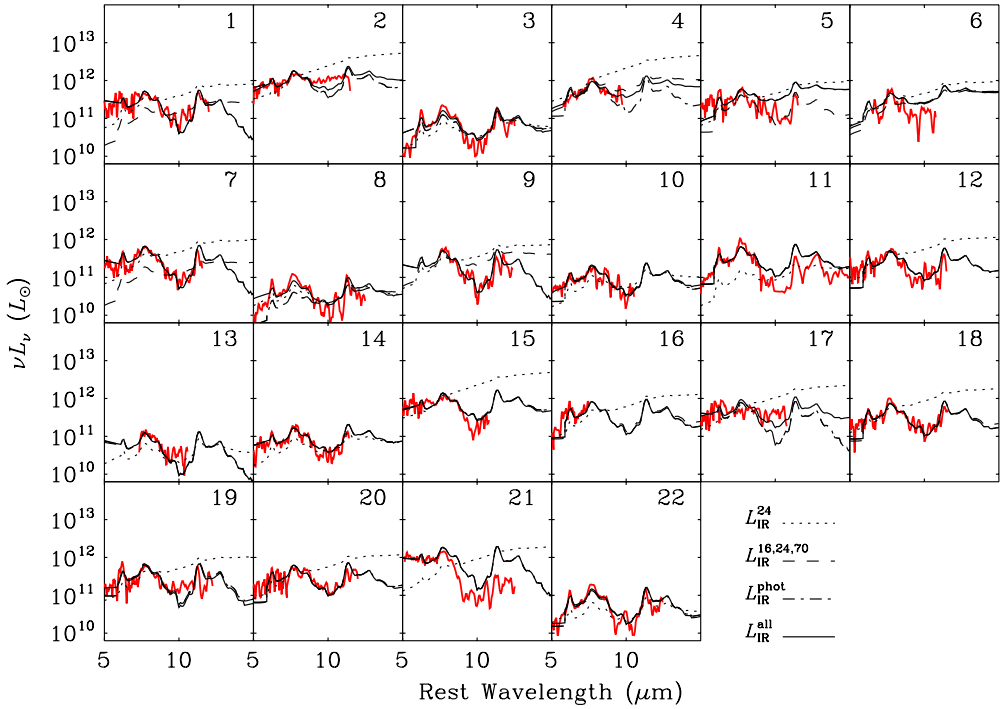

Figure 3. Blowup of the 5–15 μm range for the best-fit SEDs of Chary & Elbaz (2001) for all sources using only 24 μm flux densities (dotted lines), all three *Spitzer* (16, 24, and 70 μm) flux densities (dashed lines), *Spitzer* and submillimeter (850 μm) photometry (dot-dashed lines), and all photometry (*Spitzer* and submillimeter) along with the IRS spectra (solid lines). The actual spectra, smoothed to the instrumental resolution, are overplotted in red. The SEDs chosen when fitting with the 24 μm data alone rarely characterize the observed PAH emission as compared to when longer wavelength data are included in the fitting.

(A color version of this figure is available in the online journal.)

The mid-infrared AGN fractions are given for each galaxy in Table 4.

Next, to characterize the fraction of the IR luminosity arising from an AGN, we scale the SED template of Mrk 231 (a nearby ULIRG whose IR luminosity is known to be dominated by an AGN; Armus et al. 2007) to the AGN fraction of the rest-frame ~5–12 μm luminosity (i.e., the luminosity in the rest-frame wavelength range having IRS coverage per source) and integrate the SED from 8 to 1000 μm. This is illustrated in Figure 4 where we show the best-fit Chary & Elbaz (2001) SED for GN-IRS 7 along with the observed IRS spectra, the scaled SED of Mrk 231 (i.e., the AGN contribution), and the difference between the best-fit SED and the scaled SED of Mrk 231 (i.e., the contribution by star formation alone). The observed mid-infrared spectra clearly match the shape of the best-fit SED.

The values of $L_{\rm IR}^{\rm AGN}$ are given for each galaxy in Table 4. By subtracting these values from the IR luminosities obtained through our SED fitting, we can estimate the amount of IR luminosity arising from star formation alone such that

$$\left(\frac{\rm SFR_{IR}^{noAGN}}{M_\odot {\rm yr}^{-1}}\right) = 1.73 \times 10^{-10} \left(\frac{L_{\rm IR}^{\rm all,noAGN}}{L_\odot}\right), \qquad (8)$$

where $L_{\rm IR}^{\rm noAGN} = L_{\rm IR}^{\rm all} - L_{\rm IR}^{\rm AGN}$. Similarly, we can also calculate an AGN-subtracted SFR from the 24 μm data by SED fitting the 24 μm photometry after first subtracting off AGN fractions extrapolated from those given in Table 4; the corresponding IR luminosities and SFRs are denoted as $L_{\rm IR}^{\rm 24,noAGN}$ and $\rm SFR_{IR}^{24,noAGN}$, respectively. We have assumed that the underlying mid-infrared continuum arises purely from an AGN, however, hot dust associated with vigorous star formation may also contribute to the mid-infrared continuum emission as well. Therefore, the mid-infrared AGN fractions, and associated estimates for the IR luminosities of the AGN, should all be considered conservative upper limits.

4. RESULTS

We now present the results for the various SED fitting methods among the sample while looking for trends with redshift. In doing so, we also compare the infrared-based SFRs to those estimated from extinction-corrected UV emission for galaxies having redshifts between $1.4 \lesssim z \lesssim 2.6$.

4.1. Accuracy of Derived IR Luminosities

In Figure 2, we plot the best-fitting Chary & Elbaz (2001) SEDs for three sources (GN-IRS 2, 4, and 15) to illustrate the three fitting methods. While the addition of the IRS spectra and submillimeter data to the available *Spitzer* 16, 24, and 70 μm photometry does not seem to significantly alter the choice of the fit, the fits using 24 μm flux densities alone are highly discrepant. Zooming in on the 5–15 μm mid-infrared regions of the four different Chary & Elbaz (2001) fits for each galaxy in Figure 3, one easily sees that by using 24 μm flux densities alone the equivalent widths of the aromatic features observed in the IRS spectra are underestimated by the Chary & Elbaz (2001) templates, resulting in highly discrepant estimates of IR luminosity.

The range of IR luminosities derived by fitting the 24 μm photometry alone span a range between 4.3×10^{11} and $4.2 \times 10^{13} L_\odot$ (i.e., nearly 2 orders of magnitude) with a median of $7.5 \times 10^{12} L_\odot$. Looking at the best-fit estimates for the IR luminosities among the entire sample, we find that they range between 3.2×10^{11} and $1.1 \times 10^{13} L_\odot$ (i.e., a factor of ~35) having a median of $2.2 \times 10^{12} L_\odot$. The 24-$\mu$m-derived IR

Table 5
X-ray and UV Luminosities

ID (1)	$\log L_{0.5-8.0\,\mathrm{keV}}$ ($L_\odot$) (2)	$\log L_{2.0-8.0\,\mathrm{keV}}$ ($L_\odot$) (3)	$\log L_{\mathrm{UV}}$ ($L_\odot$ Hz^{-1}) (4)	$\log L_{\mathrm{UV}}^{\mathrm{corr}}$ ($L_\odot$ Hz^{-1}) (5)	β
1	10.16	10.13	< -5.50	< -5.50	...
2	<8.91	<9.14	−4.74	−3.23	−0.47
3	8.14	<8.03	< -4.94	< -4.94	...
4	9.59	9.49	−5.11	−3.09	0.14
5	<8.75	<8.94	< -5.43	< -5.43	...
6	<8.85	<9.07	< -5.32	< -5.32	...
7	<8.64	<8.84	< -5.44	< -5.44	...
8	7.96	7.86	< -4.78	< -4.78	...
9	8.67	8.72	−4.85	−3.46	−0.61
10	9.79	9.48	< -4.41	< -4.41	...
11	8.69	<8.47	−4.83	−2.96	−0.03
12	<8.81	<9.04	−4.98	−3.76	−0.82
13	<7.85	<8.05	−5.20	−3.18	0.14
14	8.12	<8.16	−6.18	−3.69	0.71
15	<8.98	<9.24	−5.18	−4.04	−0.91
16	8.43	<8.56	< -5.59	< -4.04	< -0.42
17	<8.80	<9.05	−4.23	−3.96	−1.95
18	8.97	8.94	−4.57	−2.53	0.18
19	8.75	8.73	< -5.53	< -5.53	...
20	<9.24	<9.49	< -5.50	< -2.69	<1.09
21	9.23	9.20	−5.55	−2.48	1.40
22	<7.87	<8.07	< -5.60	< -5.60	...

Notes. Column (1): source ID. Column (2): *K*-corrected full band (0.5–8.0 keV) luminosities. Column (3): *K*-corrected hard band (2.0–8.0 keV) luminosities. Column (4): linearly interpolated 1500 Å specific luminosities. Column(5): extinction-corrected 1500 Å specific luminosities. Column(6): slope of the UV continuum between 1250 and 2600 Å which is used to estimate extinction following Meurer et al. (1999).

luminosity is a factor of ∼4 larger than that for the best-fit estimates, on average.

Using our best-fit IR luminosities, we also note that 16 out of the 22 sample galaxies are classified as ULIRGs while the remaining six are LIRGs. Looking at the differences between the 24 μm to our best-fit IR luminosities, the discrepancy is found to be much larger among the ULIRGs than for the LIRGs. The 24-μm-derived IR luminosities are larger than the best-fit IR luminosities by a factor of ∼5, on average, for the ULIRGs while being only ∼1.2 times larger, on average, for the LIRGs.

4.2. Strength of PAH Features

To quantify how well the mid-infrared spectral features are matched by the various SED fitting methods, we compare the ratio from the peak of the 7.7 μm PAH feature to the median flux density in the 9–11 μm trough region (i.e., 9.7 μm silicate absorption feature). Given that the wavelength coverage varies for each object, making it difficult to properly estimate the true continuum levels (e.g., Pope et al. 2008a), we choose to compare this ratio rather than actual PAH equivalent widths. Furthermore, choosing these features enables us to calculate this ratio for nearly the entire sample; we do not have spectroscopic coverage over the rest-frame 9–11 μm region for GN-IRS 16.

When fitting the SEDs using the 24 μm photometry alone the peak-to-trough ratios are $\sim 0.24 \pm 0.15$ times the peak-to-trough ratios measured for the observed spectra (i.e., a factor of ∼4 times smaller), on average. By instead fitting the SEDs using all of the photometric data, the peak-to-trough ratios are now $\sim 0.75 \pm 0.84$ times the ratios of the actual data (i.e., ∼35% smaller), on average. Similarly, when the mid-infrared spectra are included in the fitting with all of the photometric data, the peak-to-trough ratios are found to be $\sim 0.75 \pm 0.58$ times the ratios for the observed spectra, on average, suggesting that fitting with mid-infrared and FIR photometry alone does a reasonable job choosing templates with the correct mid-infrared spectral features. Consequently, it appears that the improper estimates of IR luminosities from fitting with 24 μm photometry alone are most likely due to the fact that local high-luminosity galaxies do not exhibit large PAH equivalent widths relative to galaxies of similar luminosity at higher redshifts. This result is consistent with that of Desai et al. (2007) who showed that local ULIRGs typically have PAH equivalent widths that are significantly smaller than those measured for ULIRGs at high redshift. Since the strongest PAH features, lying in between 6 and 12 μm, begin to redshift into the observed 24 μm band at $z \gtrsim 1.4$, we expect the discrepancies between the fitting methods and estimates for the IR luminosity of galaxies, to increase with increasing redshift. For the sample galaxies in the redshift range between $1.4 \lesssim z \lesssim 2.6$, we find that the peak-to-trough ratios of the SEDs chosen by fitting the 24 μm data alone and using all of the available photometric data are an average factor of $\sim 0.19 \pm 0.11$ (i.e., ∼5 times smaller) and $\sim 0.88 \pm 0.94$ (i.e., ∼14% smaller) times those measured for the data, respectively.

We also note that by remeasuring the peak-to-trough ratios of the best-fit SEDs after subtracting the fitted AGN component, the median ratios are $\sim 1.11 \pm 0.30$ and $\sim 1.49 \pm 0.42$ for the entire sample and galaxies at $z \gtrsim 1.4$, respectively. This result demonstrates that the AGN/star-formation decomposition is fairly reliable and that, as previously stated, we likely overestimate the true AGN contribution by assuming that all of the mid-infrared continuum emission arises from hot dust associated with the AGN. These statistics exclude three galaxies (GN-IRS 1, 13, 17) for which the AGN component oversubtracts the continuum of the best-fit SEDs resulting in a negative peak-to-trough ratio. Including them in the above calculations does not affect the median values, but increases the dispersion significantly.

4.3. Redshift Dependency

In Figure 5, we plot L_{IR}^{24}, $L_{\mathrm{IR}}^{\mathrm{all}}$, and $L_{\mathrm{IR}}^{\mathrm{RC}}$ versus redshift for the 70 μm detected galaxies. Although the different IR luminosity estimates largely agree for the $z < 1.4$ sources, the three sources at $z > 1.4$ have IR luminosities derived from fitting the 24 μm flux densities alone that are larger by an average factor of ∼4 than what is found when fitting the SEDs with all available data.

Since the 70 μm detections could potentially be sampling objects with the warmest FIR dust color temperatures, we also compare the different IR luminosity estimates of all sources in our sample in Figure 6. We find a significant change in this ratio with redshift. While the objects near $z \sim 1$ all have ratios around unity, galaxies in a redshift range between $1.4 \lesssim z \lesssim 2.6$ exhibit ratios of $\sim 4.6 \pm 1.4$, on average. We also note that galaxies lying at redshifts below and above $z \sim 1.4$ typically have L_{IR}^{24} values below and above $\sim 3 \times 10^{12} L_\odot$, respectively. This result is consistent with that of Papovich et al. (2007) whom report that IR luminosities derived from stacking 70 and 160 μm data for a sample of 24 μm bright (i.e., $f_\nu(24\ \mu\mathrm{m}) > 250\ \mu$Jy) galaxies lying in a redshift range between $1.5 \lesssim z \lesssim 2.5$, are a factor of 2–10 lower than those inferred from using only 24 μm flux densities. A similar comparison with the radio continuum based luminosities over the same redshift range shows that the 24 μm based IR luminosities are higher by a factor of $\sim 1.5 \pm 1.9$, on average.

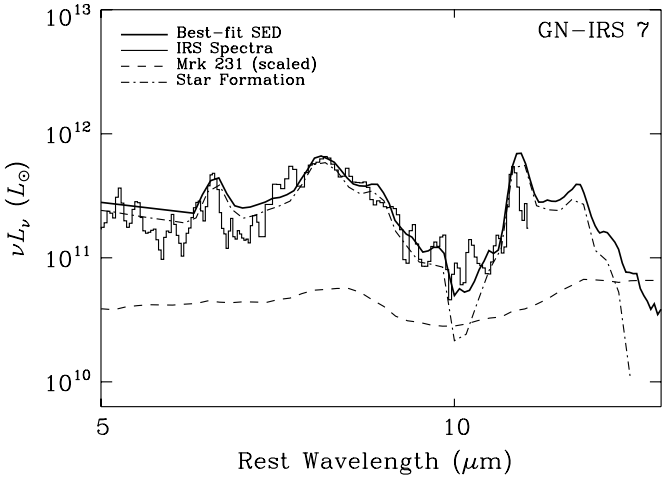

Figure 4. Best-fit SEDs of Chary & Elbaz (2001) for GN-IRS 7 plotted as the bold solid line, given in the rest-frame. Overplotted are the IRS spectra of the source (solid histogram-style line), the scaled Mrk 231 template (dashed line), corresponding to the contribution to the SED by the AGN, and the contribution to the SED by star formation (dot-dashed line).

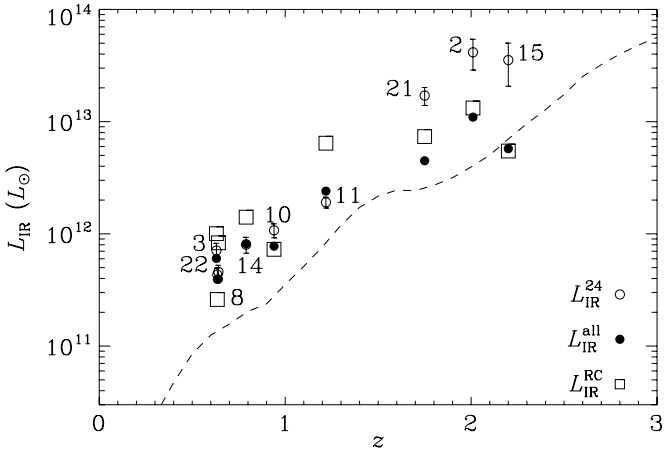

Figure 5. Plot of IR luminosity, estimated by three different means, vs. redshift for galaxies in our IRS sample which have 70 μm detections; associated 1σ error bars are given. L_{IR}^{24} values (open circles) are calculated by SED template fitting using the 24 μm flux density only while L_{IR}^{all} values (filled circles) also include the 16, 70, and 850 μm photometry (where available) along with IRS spectra. L_{IR}^{RC} values are calculated using the well-known FIR–radio correlation and plotted as open squares; since the uncertainties associated with these estimates are large (i.e., a factor of ∼2), we do not plot error bars. The L_{IR}^{24} estimated by SED fitting the sample's f_ν(24 μm) flux density limit of 220 μJy as a function of redshift is plotted as the dashed line.

It is unclear if this discrepancy is due to the flux limit of our sample which implies that we are sampling sources with high luminosities at $z \sim 2$ for which no local analogs exist. This would suggest that the extrapolation of the local SEDs to these high-redshift sources is invalid. A second possibility is that $z \sim 2$ sources have sufficiently low metallicities that the infrared SEDs deviate from those of $z \sim 1$ or local galaxies. A third possibility that has been suggested is that warm dust continuum emission from an obscured AGN in these sources is biasing the 24 μm flux upward and resulting in overestimates of the SFR (Daddi et al. 2007a).

4.4. AGN-subtracted SFR Estimates from 24 μm

The SFRs inferred from the 24-μm-derived IR luminosities overestimate those inferred from our best-fit IR luminosities,

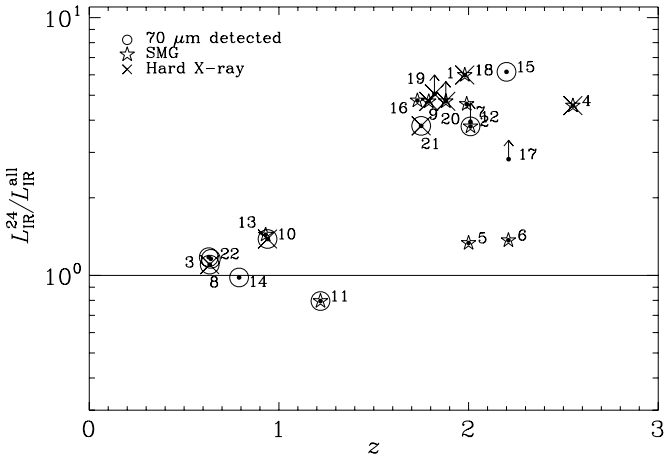

Figure 6. Plot of the ratio between the 24-μm-derived IR luminosity (L_{IR}^{24}) to that derived using the additional constraints from the IRS spectroscopy along with the 16, 70, and 850 μm data. Sources having hard band (2.0–8.0 keV) X-ray detections are identified with an "×." For sources not identified at 70 and 850 μm, we plot an upward arrow indicating that the IR luminosity is only an upper limit.

corrected for any contributions from AGN (SFR_{IR}^{noAGN}; see Section 3.5) by a factor of ∼6, on average, among the entire sample. To see whether this overestimation by fitting the 24 μm photometry is the result of excess mid-infrared emission arising from hot-dust emission associated with the presence of an AGN, we refit the 24 μm flux densities to the SED templates after correcting them by the corresponding mid-infrared AGN fraction. We find that SFRs calculated using IR luminosities derived by SED fitting 24 μm flux densities after subtracting the mid-infrared AGN contributions are $\sim 2.5 \pm 2.3$ times larger, on average, than the values of SFR_{IR}^{noAGN} among the entire sample. There also appears to be a redshift dependence such that the SFRs calculated using IR luminosities derived by SED fitting 24 μm flux densities after subtracting the mid-infrared AGN contributions are $\sim 1.0 \pm 0.4$ and $\sim 3.3 \pm 2.2$ times larger, on average, than the values of SFR_{IR}^{noAGN} for galaxies at redshifts below and above $z \sim 1.4$, respectively.

We believe that IR luminosities are overestimated by fitting local SEDs to 24 μm photometry alone because of differences in PAH equivalent widths among galaxies of similar luminosity at different redshifts. This conclusion is supported by our findings in Section 4.2 where we compared the observed PAH strengths to those from the different SED fits. Alternatively, this result could also imply that using Mrk 231 to approximate the AGN component is inappropriate. However, given that we believe our mid-infrared AGN fractions and IR luminosity estimates for the AGN to be conservative upper limits, this is unlikely to be a dominant effect.

4.5. Multiwavelength Comparison Between SFR Estimates

In order to assess the reliability of the different SFR indicators, we make a cross comparison between the UV, radio, and IR SFR estimates. We examine how these estimates compare for galaxies located at redshifts below and above $z \sim 1.4$.

4.5.1. $z < 1.4$ Galaxies

For the seven galaxies located at $z < 1.4$, we find that SFRs inferred from their 24 μm data alone range from being ∼0.8 to ∼1.4 times that of those SFRs calculated using our best-fit IR luminosities, and are only 16% larger, on average. However,

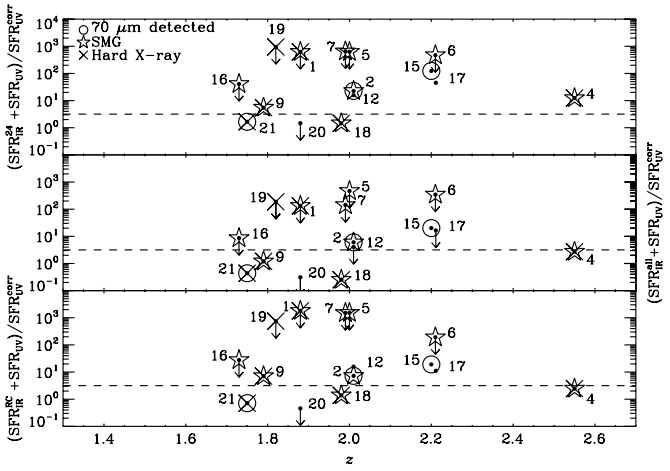

Figure 7. Top panel: plot of the ratio of SFRs estimated from the 24 μm flux densities (plus a nonobscured UV-derived SFR) to extinction-corrected UV SFRs as a function of redshift. The dashed line indicates where the logarithm of this ratio is equal to 0.5 dex; galaxies taking values larger than this are considered to be "mid-infrared excess" sources (i.e., Daddi et al. 2007a). Sources undetected in the optical, such that its UV slope could not be fit, are plotted with downward arrows. In the middle panel, we plot the same ratio vs. redshift, except that we use all available data to derive the IR-based SFRs (SFR_{IR}^{all}). The IR-based SFRs are considered to be upper limits for those galaxies not detected at 70 and 850 μm The same is done again in the bottom panel, except that we use the 20 cm radio continuum flux densities and the FIR–radio correlation to derive SFRs (SFR_{IR}^{RC}). Mid-infrared excess sources largely remain even when the bolometric corrections are accounted for.

using the radio data to infer a SFR via the FIR–radio correlation, we find that the radio SFRs overestimate those calculated using the best-fit IR luminosities by a factor of ∼1.7, on average, and range from being a factor of ∼0.7 to ∼2.7 times that of the SFRs measured using are best-fit IR luminosities. Among these seven galaxies, only three have measurable UV slopes allowing us to calculate a UV-corrected SFR. These SFRs range from being a factor of ∼0.8 to ∼6.5 times that of the SFRs measured using our best-fit IR luminosities.

4.5.2. $z > 1.4$ Galaxies

Daddi et al. (2007a) have identified discrepancies between the UV, radio, and IR-derived SFR estimates in $z \sim 2$ galaxies selected using the BzK selection technique. We select the 15 galaxies in our sample with $1.4 \lesssim z \lesssim 2.6$ which matches the redshift range spanned by the BzK selection. Figure 7 shows the ratio of SFRs inferred from the 24 μm data (plus the uncorrected UV-based SFR) to those estimated from extinction-corrected UV measurements for these 15 galaxies. Galaxies which are not detected in the optical, such that their UV slopes could not be estimated, are plotted as upper limits although they are difficult to interpret. Their best-fit IR-derived SFRs are nearly 2 orders of magnitude larger than the uncorrected UV-based SFRs, on average. However, their extinction-corrected UV SFRs could potentially be very large, reducing the plotted ratio.

Daddi et al. (2007a) defined sources for which

$$\log\left(\frac{\mathrm{SFR_{IR}} + \mathrm{SFR_{UV}}}{\mathrm{SFR_{UV}^{corr}}}\right) > 0.5 \qquad (9)$$

to be "mid-infrared excess" sources. While the numerator adds the contribution of energetic emission from young massive stars that is not absorbed and reemitted by dust grains to obtain a total SFR, the extincted UV SFR is often negligible compared to the IR-based SFR term.

Not surprisingly, we find that all seven galaxies for which we do not have UV slope measurements, and thus cannot make UV extinction corrections, all meet the mid-infrared excess criterion. For these sources to fall below the mid-infrared excess criterion would require an average extinction of $A_V \gtrsim 1.7$ mag; and to fall to a ratio near unity requires an average extinction of $A_V \gtrsim 2.2$ mag. As for the remaining eight sources, we find that six are identified as having mid-infrared excesses: GN-IRS 2, 4, 9, 12, 15, and 17.

The two sources for which we do not find any mid-infrared excess, due to their steep UV corrections, are GN-IRS 18 and 21. Both GN-IRS 18 and 21 are X-ray detected, however, GN-IRS 18 is also an SMG. Morphologically, GN-IRS 18 appears extended possibly due to a major merger event. The extinction estimated for GN-IRS 18 is $A_V \approx 1.92$ mag, only 0.16 mag larger than the median extinction found for all sample galaxies for which the rest-frame UV slope could be measured. The extinction estimated for GN 21, however, is the largest among the entire sample at $A_V \approx 2.89$ mag. While their optical extinctions differ significantly, these are the only two sources having extinction-corrected UV SFRs in excess of 1000 $M_\odot$ yr^{-1}.

By plotting again the ratio of IR + UV to UV-corrected SFRs, this time instead using our best-fit IR luminosities, versus redshift in the middle panel of Figure 7, we find that two of the six previously identified mid-infrared excess galaxies (GN-IRS 4 and 9) are no longer mid-infrared excess sources. These two galaxies are also the only ones among the six to have hard X-ray detections. In fact, only two sources, GN-IRS 2 and 15, seem to remain definitive "mid-infrared excess" galaxies given that GN-IRS 12, which barely lies above the mid-infrared excess threshold, and GN-IRS 17 are not detected at either 70 or 850 μm implying that their associated best-fit IR luminosities are technically upper limits. If, on the other hand, we use the radio continuum based SFRs to construct the same plot, as shown in the bottom panel of Figure 7, we find that while points have shifted downward, only GN-IRS 4 is no longer considered a mid-infrared excess source leaving five of the original six mid-infrared excess galaxies above the threshold.

To summarize, we find that by using the best-fit IR luminosities we can definitively account for 2/6 mid-infrared excess sources (i.e., 1/3 of those found using 24 μm derived IR luminosities). This fraction is increased to 2/3 by assuming that we are still overestimating the IR luminosities of the two galaxies for which we only have upper limits at FIR wavelengths. The median ratio of best-fit IR to extinction-corrected UV SFRs for sources in the redshift range between $1.4 \lesssim z \lesssim 2.6$ is ∼4. By instead using the radio continuum and FIR–radio correlation to derive IR luminosities, the median ratio between the radio derived-to-extinction-corrected UV SFRs is even larger at ∼7. We investigate in the discussion below whether the contribution from an obscured AGN is large enough to account for the discrepancy between the IR and UV SFR estimates among these sources.

5. DISCUSSION

Using IRS spectroscopy along with additional photometric data, we have set out to characterize better the IR properties for a diverse sample of 24 μm selected sources. In doing this we also try to explain the true nature of sources considered to have an excess of IR emission relative to their ultraviolet luminosity when 24 μm photometry, alone, is used to estimate SFRs. Specifically, through a spectral decomposition of the IRS

Table 6
Summary of Sources

ID	Class[a]	Comment
1	AGN	UV-slope indeterminate
2	CT-AGN	Mid-infrared excess even after AGN subtraction and proper bolometric correction
3	SF	Strong PAH Features; UV-slope indeterminate
4	SF	Strong PAH features; UV-slope underestimates extinction
5	SF	UV-slope indeterminate
6	SF	UV-slope indeterminate
7	SF	Strong PAH features; UV-slope indeterminate
8	SF	Strong PAH features; UV-slope indeterminate
9	SF	UV-slope correctly estimates extinction
10	SF	UV-slope indeterminate
11	SF	Strong PAH features; UV-slope correctly estimates extinction
12	SF	Strong PAH features; UV-slope underestimates extinction; low $q_{\rm IR}$ value
13	SF	UV-slope overestimates extinction
14	SF	UV-slope correctly estimates extinction
15	CT-AGN	Mid-infrared excess even after AGN subtraction and proper bolometric correction
16	SF	Strong PAH features
17	CT-AGN	Mid-infrared excess even after AGN subtraction and proper bolometric correction
18	SF	Strong PAH features; UV-slope overestimates extinction
19	SF	Strong PAH features
20	SF	UV-slope indeterminate
21	AGN	UV-slope and 24 μm conspire to produce consistent SFRs
22	SF	Strong PAH features; UV-slope indeterminate

Note.
[a] Final classification: AGN, IR AGN fraction larger than 50%; CT-AGN, Compton-thick AGN; SF, star formation dominated source.

data, we determine that half of the "mid-infrared excess" sources are Compton-thick AGNs. A summary of our findings for each of the 22 sample galaxies is given in Table 6.

5.1. Discrepancies in SFR Estimates Versus the Contribution from AGN

As discussed in Section 4.5.2, we find that even after using the best-fit IR luminosities, $L_{\rm IR}^{\rm all}$, to derive SFRs, we still find 4/8 sources in the redshift range between $1.4 \lesssim z \lesssim 2.6$ with measurable UV slopes to exhibit excesses in the infrared relative to what is measured by extinction-corrected UV data (middle panel of Figure 7). To see if the observed excess is in fact due to the presence of an obscured AGN, we estimate the fraction of AGN power contributing to the total IR luminosity using our mid-infrared spectroscopy as described in Section 3.5.

In the left panel of Figure 8 we plot the ratio of our best-fit IR derived SFRs, plus an unobscured UV component, to the extinction-corrected UV SFRs against the mid-infrared AGN fractions before and after subtracting the AGN contribution to the total IR luminosity. We find that 3/8 galaxies having redshifts between $1.4 \lesssim z \lesssim 2.6$ and which continue to exhibit an excess of IR emission have mid-infrared AGN fractions that are larger than 60%. Using the Mrk 231 SED as outlined in Section 3.5, we can estimate the contribution of AGNs to the total IR luminosity.

Looking at the entire sample (i.e., all 22 galaxies), we find that AGNs account for ∼30% of the total IR luminosity, on average, with a range of ∼10%–70% (Table 4). This is similar to the average AGN contribution of ∼30% we find among the hard band X-ray detected sources. Interestingly, we also find that the average contribution to the total IR luminosity by AGN is also ∼30% for both subsamples of SMGs and non-SMGs. This contribution by the AGN to the IR luminosity of SMGs is a factor of ∼2 times larger than that reported by Pope et al. (2008a) which we attribute to the differences in the IR luminosities arising from differences in the SED fitting methods; as previously stated, Pope et al. (2008a) included the radio photometry in their SED fitting leading to IR luminosities typically larger than those presented here.

In the right panel of Figure 8, we plot AGN luminosity versus the difference between the 24 μm and best-fit estimate IR luminosities. A clear trend of increasing AGN luminosity with increasing overestimation of the IR luminosity using 24 μm photometry alone is observed; or, in other words, AGN luminosity appears to scale with increasing mid-infrared luminosity. Performing an ordinary least-squares fit to the data, we find that

$$\log\left(\frac{L_{\rm IR}^{\rm AGN}}{L_\odot}\right) = (0.50\pm0.04)\log\left(\frac{L_{\rm IR}^{24}-L_{\rm IR}^{\rm all}}{L_\odot}\right)+(5.61\pm0.52). \quad (10)$$

While the differences between the 24 μm and best-fit IR luminosities are large for galaxies having large (i.e., $\gtrsim$60%) mid-infrared AGN fractions, we find these quantities to be unrelated for galaxies having smaller mid-infrared AGN fractions. We also find that the AGN luminosity accounts for only 16% of the difference between the 24 μm derived and best-fit IR luminosities, on average. This indicates that the AGN contribution to the mid-infrared excesses, which would result in overestimates of IR-based SFRs, is close to negligible when compared to the improper bolometric correction applied when estimating total IR luminosities by fitting local SED templates with 24 μm data alone. As shown in Section 4.4, SFRs derived by subtracting the AGN fraction from the 24 μm photometry are larger than the AGN-corrected best-fit IR SFRs by a factor of ∼1 to ∼3.3, on average for redshifts below and above $z \sim 1.4$, respectively. Furthermore, the AGN-corrected 24 μm SFRs are factors of ∼1 to ∼68 times larger than the corresponding UV-corrected SFRs for sample galaxies at redshifts above $z \sim 1.4$. Therefore, the AGN is not the dominant source of the inferred "mid-infrared excesses" among these systems.

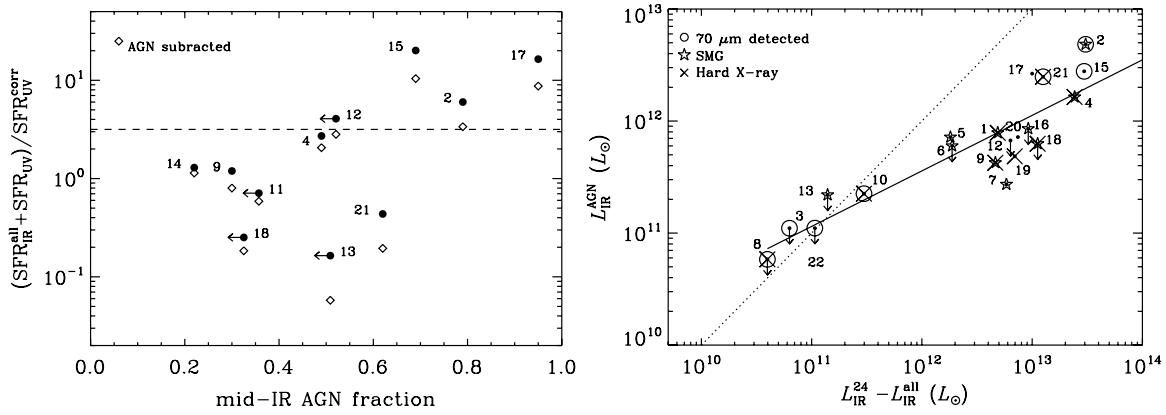

Figure 8. Left panel: plot of the ratio of IR-derived SFRs using our best-fit IR luminosities, plus an unobscured UV component, to extinction-corrected UV SFRs vs. the mid-infrared AGN fraction before and after subtracting the AGN contribution to the total IR luminosities using filled circles and open diamonds, respectively. The dashed line indicates where the logarithm of this ratio is equal to 0.5 dex; galaxies taking values larger than this are considered to be "mid-infrared excess" sources (i.e., Daddi et al. 2007a). In the right panel, we plot the estimated AGN luminosity (see Section 3.5) as a function of the difference between the 24 μm and best-fit IR luminosities. Sources for which only upper limits to the AGN mid-infrared luminosity fraction could be determined are shown as downward arrows. An ordinary least-squares fit is overplotted as a solid line while the dotted line indicates a one-to-one relationship to show that the AGN luminosity is not able to account for the difference in the bolometric correction when fitting the SED templates with 24 μm photometry alone.

Since the FIR–radio correlation is thought to solely arise from the processes associated with massive star formation, we looked to see if the IR/radio ratios themselves are sensitive to the fractional AGN power by comparing the ratio of $L^{AGN}_{IR}/L^{all}_{IR}$ with q_{IR} values. A trend was not found suggesting that q_{IR} is insensitive to the fractional IR output by the AGN. This result likely arises because the AGN contributes to the radio and infrared emission by different amounts.

5.1.1. The Persistence of "Mid-Infrared Excess" Sources

By subtracting off our estimate of the AGN contribution to the total IR luminosity, we determine whether this is enough to account for the remaining IR excesses for galaxies in Figure 7. We recreate the top and middle panels of Figure 7 in the top and bottom panels of Figure 9, respectively, by computing the 24-μm-derived and best-fit IR-based SFRs after subtracting off the estimated AGN contribution for the eight galaxies having optical detections which allowed for proper estimates of extinction-corrected UV SFRs; the decrease in IR SFRs is indicated by vertical lines.

Among these sources we find that $(L^{24}_{IR} - L^{24,noAGN}_{IR})/L^{24}_{IR}$ and $(L^{all}_{IR} - L^{all,noAGN}_{IR})/L^{all}_{IR}$ are both ∼45%, on average. However, even by using the AGN-corrected 24 μm SFRs, none of the previously identified mid-infrared excess sources are removed. While the AGN fractions are similar in both cases, the AGN-subtracted 24 μm SFRs are still ∼6 times larger, on average, than the AGN-corrected SFRs using the best-fit IR luminosities. In the bottom panel of Figure 9 we find that by subtracting the AGN luminosities we are able to account for the observed IR excesses in only one more source; GN-IRS 12, which is plotted as an upper limit, is now no longer considered to have excess IR emission. Therefore, of the eight sources with optical detections such that we can estimate a UV extinction correction in the redshift range between $1.4 \lesssim z \lesssim 2.6$, 6 of which would be classified as "mid-infrared excesses" using 24 μm-based IR SFRs, three (GN-IRS 2, 15, and 17) remain mid-infrared excess sources even after the subtraction of the AGN component.

Ultimately, we find that even after correcting for the presence of an AGN, the IR-based SFRs are a factor of ∼2.8 times larger, on average, than those derived from extinction-corrected UV measurements for $1.4 \lesssim z \lesssim 2.6$ galaxies with secure estimates of their rest-frame UV slopes. Or, in other words, AGNs are only able to account for ∼35% of the excess IR emission measured, on average. Since we do not believe our IR luminosities are overestimated by such a large amount, given the small uncertainties associated with our SED fitting, we interpret this result to suggest that using the UV slope to derive an extinction correction is not appropriate for the entire sample; extinctions are underestimated thereby yielding underestimates for the UV-derived SFRs. This may not be too surprising given that there are catastrophic failures using the rest-frame UV slope to derive the extinction for galaxies having both low and high extinctions. If extinction within a galaxy is too high, this method will fail simply because the galaxy's ISM will become optically thick. In the case of low extinction the UV slope will no longer be as sensitive to the amount of extinction since variations arising from contributions by a galaxy's old stellar population will become important (Reddy et al. 2006).

5.1.2. AGN-Dominated Sources

Of the remaining three mid-infrared excess sources after correcting for the contribution of the AGN to the total IR luminosity, GN-IRS 17 is the only source plotted as an upper limit, however all have mid-infrared AGN fractions $\gtrsim$60% suggesting that they are AGN dominated. While the remaining IR excess for GN-IRS 17 may arise from improper SED fitting due to only having upper limits at 70 and 850 μm, we note that its optical morphology is point-like and consistent with being an AGN. It may then be that the SED templates used for the fitting, which are based on star-forming galaxies, are not appropriate resulting in an incorrect estimate of the total IR luminosity. In fact, this source has recently been identified as a Compton-thick AGN by Alexander et al. (2008a). Similarly, GN-IRS 2 is thought to be a Compton-thick AGN (Pope et al. 2008a), so it is not surprising to find that it lies above the threshold even though it is not plotted as an upper limit. Thus, the only remaining mid-infrared excess source which is not plotted as an upper limit or has not been previously identified as a Compton-thick AGN is GN-IRS 15.

Inspecting the IRS spectra for this source, it shows strong evidence of a deep silicate absorption feature and weak PAH equivalent widths, suggestive of a deeply embedded AGN. The

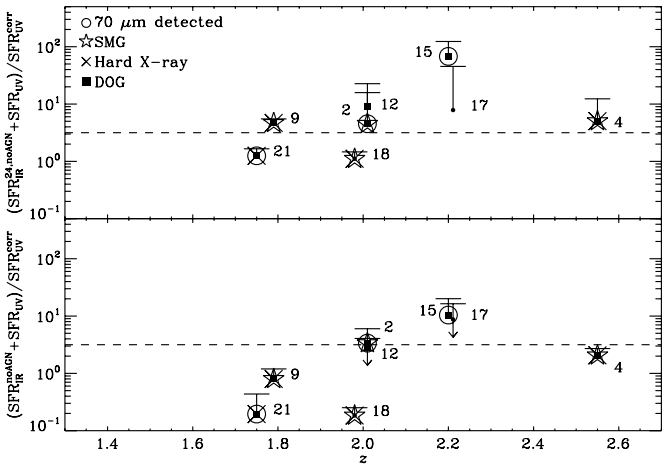

Figure 9. Top panel is similar to that of the top panel of Figure 7, except that we have subtracted the AGN fraction from the 24 μm photometry before calculating the associated IR luminosities and SFRs. We also only show galaxies for which a proper extinction-corrected UV SFR could be calculated. The decrease, which is ∼45% on average among these sources, is shown by a vertical line. In the bottom panel we subtract the AGN contribution to our best estimates of the IR luminosity (i.e., $L_{\rm IR}$ values estimated from SED fitting all available data to derive SFRs). The decrease in SFR by correcting for the AGN (∼45% on average among these sources as well) is again shown by a vertical line. While the decrease to the SFRs by correcting for AGN is similar among these sources, the AGN-subtracted 24 μm SFRs are still ∼6 times larger, on average, than the AGN-corrected SFRs from our best-fit IR luminosities.

ACS imagery of this source is also point-like, which too seems consistent with the source being an AGN. Consequently, we believe that GN-IRS 15 is primarily powered by an AGN (i.e., a Compton-thick AGN) for which our SFR estimates are not physically meaningful.

The other source which appears to be clearly AGN dominated according to its mid-infrared AGN fraction is GN-IRS 21. We note that this source never appears to be a mid-infrared excess source even when comparing its UV-corrected SFR to that derived from SED fitting 24 μm photometry. However, by attempting to correct for the AGN in this source, we find that the best-fit IR derived SFR becomes ∼5 times smaller than that of the UV-corrected SFR; clearly the UV and IR SFR estimates for this AGN dominated source are not physically meaningful. We also note that GN-IRS 4 and 12, which just barely drop below the mid-infrared excess threshold in the bottom panel of Figure 9, have mid-infrared AGN fractions near 50%. However, since our mid-infrared AGN fractions are considered to be upper limits, we believe these systems to likely be dominated by star formation.

Of the six originally identified "mid-infrared excess" sources, based on extrapolating IR-based SFRs from SED fitting 24 μm photometry alone, three remain even after accounting for the presence of AGN and applying proper bolometric corrections. This suggests that the sky and space densities of Compton-thick AGNs reported by Daddi et al. (2007b) likely overestimate the true values by a factor of ∼2, yielding corrected values of ∼1600 deg^{-2} and ∼1.3 × 10^{-4} Mpc^{-3}, respectively.

5.1.3. Are "Mid-Infrared Excess" Sources DOGs?

In Figure 9, we label sources which would be identified as dust-obscured galaxies (DOGs) using the definition of Dey et al. (2008), $f_\nu(24\ \mu{\rm m})/f_\nu(R) > 982$, to see if they clearly separate out as mid-infrared excess sources. We estimate *R*-band flux densities by interpolating between the *V* and i_{775} band photometry. More than half of the sample (i.e., 13 sources, seven of which we could not measure proper extinction-corrected UV SFRs and are therefore not included in Figure 9) fit the DOG definition. Not all DOGS can be classified as mid-infrared excess sources. Conversely, not all mid-infrared excess sources are DOGs. This result is not too surprising since DOGs are thought to be powered by both star formation and AGN processes (Pope et al. 2008b). However, we do find that DOGs are only identified for sources with $z > 1.4$. In fact, 87% of our sample having a redshift greater than 1.4 are classified as DOGs.

5.2. *Application For Other Fields with Deep* Spitzer *and* Herschel *Far-infrared Imaging*

We compare the results of our SED fitting to situations when only mid-infrared photometry (e.g., at 16 and/or 24 μm) along with additional measurements at 70 μm are available. Such a comparison is especially important for the FIDEL fields, because of their deep 70 μm imaging, as well as for upcoming dedicated *Herschel* programs such as GOODS-*Herschel* (GOODS-H; P.I.: D. Elbaz).

In the third panel of Figure 10 we plot the ratio of IR luminosities derived by fitting the 16, 24, and 70 μm photometry to $L_{\rm IR}^{\rm all}$ as a function of redshift. The median ratio has a value of ∼1.02 ± 0.51. We find the ratio to be approximately constant with increasing redshift, with average values of ∼1.01 ± 0.06 and ∼1.20 ± 0.61 for redshifts below and above $z \sim 1.4$, respectively, suggesting that the systematic variations introduced by the presence of strong PAH emission redshifting into the 24 μm band at $z \gtrsim 1.4$ is largely taken into account by having the additional 70 μm data point. We also see that the dispersion significantly increases with redshift. We therefore believe that using mid-infrared photometry with the addition of a 70 μm measurement provides fairly reliable estimates for the true IR luminosity compared to when fitting with the 24 μm data alone. We also note that it is the addition of the 70 μm data, and not the additional 16 μm photometry, which is responsible for the improved determination of IR luminosities.

In the first (top) panel of Figure 10 we plot the ratio of IR luminosities derived by fitting the 16 and 24 μm photometry to those using all of the available data versus redshift. The median ratio of 16+24 μm derived to our best-fit IR luminosities is ∼1.17±1.65. As with the comparison made above, the median and dispersion in the ratio of IR luminosity estimates increases with redshift, going from ∼0.99 ± 0.19 to ∼1.29 ± 1.82 at redshifts below and larger than $z \sim 1.4$. This is of course not surprising since fitting the 16 and 24 μm photometry for redshifts beyond $z \sim 1$ is complicated by the presence of PAH and silicate absorption features being redshifted into both bands. Instead, taking the ratio of 24 + 70 μm derived to our best-fit IR luminosities, we find a median ratio of ∼1.07±0.45 which is illustrated in the second panel of Figure 10. Similarly, we find the median ratio to remain near unity for galaxies below and above $z \sim 1.4$, however, the increase in the dispersion between these subsets is less significant being ∼1.04 ± 0.13 and ∼1.29 ± 0.53, respectively. Furthermore, we find that the addition of the 16 μm photometry to SED fitting the 24 and 70 μm data does not result in largely different IR luminosity estimates; the median ratio of IR luminosities from fitting the 16–70 μm data to those from fitting only the 24 and 70 μm data is ∼1.03 ± 0.29 and ranges from ∼1.03 ± 0.12 to ∼1.03 ± 0.34 for galaxies below and above $z \sim 1.4$, respectively. Such a comparison is useful since most deep fields only have coverage at 24 and 70 μm. Consequently, the addition of the 16 μm

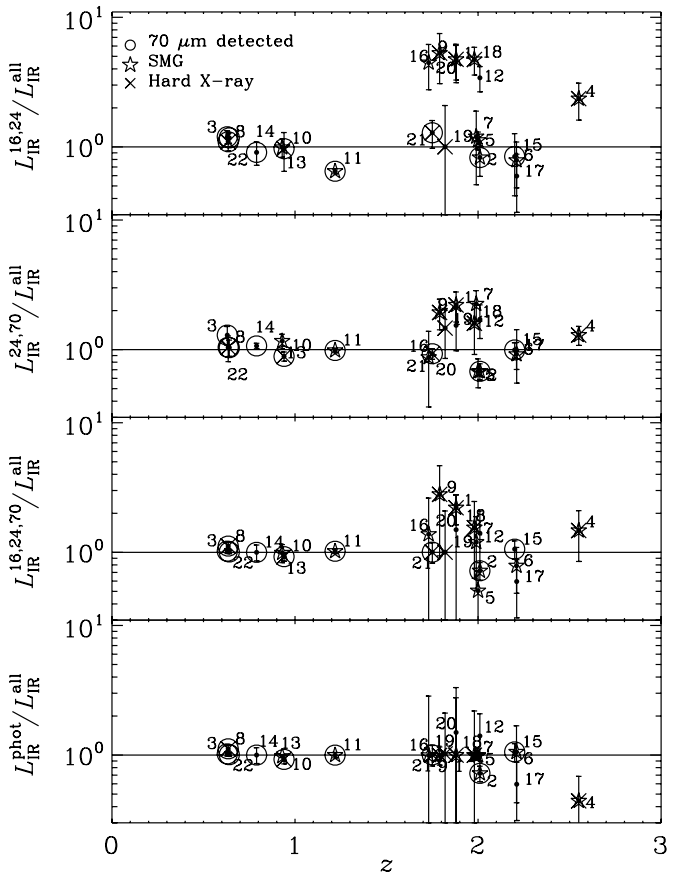

Figure 10. Top panel: plot of the ratio between the 16 and 24-μm-derived IR luminosity ($L_{IR}^{16,24,70}$) to that derived using the additional constraints from the IRS spectroscopy and 850 μm submillimeter data. Similarly, in the second and third panels, we plot the ratio of the 24 and 70-μm-derived ($L_{IR}^{24,70}$) and the 16, 24, and 70-μm-derived ($L_{IR}^{16,24,70}$) IR luminosities to those estimated from fitting all available data, respectively. In the bottom panel, we plot the ratio between IR luminosities derived from fitting all available photometric data (L_{IR}^{phot} to our best-fit IR luminosities, which also included the IRS spectra in the SED template fitting. This comparison is shown to see how well the mid-infrared spectral region is characterized by fitting photometry alone and how differences are reflected in the associated IR luminosity values. Errors in the fitting are shown. In each panel a solid line is plotted indicating a ratio of unity.

photometry does not appear to improve the fitting significantly compared with the addition of the 70 μm data.

It is interesting to see how including the mid-infrared spectra affects the SED template fitting compared to when using only the available photometry. We plot the ratio of $L_{IR}^{phot}/L_{IR}^{all}$ as a function of redshift in the bottom panel of Figure 10. We find that the ratio has a median that is approximately unity and a dispersion of $\pm$0.22. While the median of the ratio remains near unity for redshifts below and above $z \sim 1.4$, we again find that the dispersion increases with redshift, taking values of $\sim$0.06 and $\sim$0.26 in these redshift bins, respectively.

Furthermore, we find that using the 70 μm data alone to derive IR luminosities does not appear to be reliable as this method significantly underestimate the true IR luminosity. Among the 70 μm detected sources (only 2/9 which are SMGs), the best-fit IR luminosities are larger by an average factor of $\sim 1.9 \pm 0.22$ than the IR luminosities derived from the 70 μm data alone. Such a result is expected if the average galaxy at high redshift has an SED which is cooler than that of a local galaxy at the same luminosity (e.g., Pope et al. 2006; Kovács et al. 2006; Huynh et al. 2007). However, to make a conclusive statement about such an effect requires a precise sampling of the full IR SED, including the peak, which we do not have.

Seeing that the addition of 70 μm data, alone, to mid-infrared photometry yields relatively reliable estimates of IR luminosity among these galaxies, FIDEL observations (i.e., deep 70 μm imaging) of the entire GOODS-N field are used to better constrain estimates of the IR luminosity for all 24 μm detected sources having spectroscopic redshifts in E. J. Murphy et al. (2009, in preparation). By doing so, we are able to improve estimates for how the IR luminosity density evolves with redshift and characterize better the number density of mid-infrared excess sources.

5.3. The FIR–Radio Correlation

Using these data also enables us to look at the behavior of the FIR–radio correlation among a diverse group of galaxies spanning a redshift range between $0.6 \lesssim z \lesssim 2.6$. In calculating the radio-based IR luminosities and associated SFRs we have assumed that the FIR–radio correlation remains constant with redshift. We will now try to verify if such an assumption was appropriate.

5.3.1. Lack of Evolution with Redshift

In Figure 11, we plot q_{IR}, defined in Equation (1), as a function of redshift. Infrared luminosities are estimated from SED fitting using all available photometry and the IRS spectroscopy. The median q_{IR} value, plotted as dot-dashed line in Figure 11, is 2.41 ± 0.39 dex, below, but consistent with, the local value of 2.64 ± 0.26 (Bell 2003). Interestingly, we note that the four galaxies having the largest mid-infrared AGN fractions (GN-IRS 2, 15, 17, and 21) have q_{IR} values very near the canonical ratio, being within 0.18 dex, on average. This indicates that the FIR–radio correlation is a poor discriminant of obscured AGN activity.

While the correlation appears to remain linear with redshift for the few objects being studied here, more than 50% of the SMGs in this sample (i.e., 7/11) have IR/radio ratios <2.24. This is a factor of $\gtrsim$2.5 below the average value measured in the local Universe for both normal star-forming galaxies and ULIRGs. These galaxies drive the large dispersion found among the entire sample relative to what is found in the local Universe. The SMGs show a scatter in q_{IR} of 0.44 dex compared to 0.27 dex for the non-SMGs suggesting a more heterogeneous population. In contrast, 12/13 ULIRGs in the Yun et al. (2001) sample, (i.e., excluding a single, radio-loud AGN), have a median IR/radio ratio which is 33% larger than the canonical value and a dispersion of only 0.28 dex. While the average q_{IR} value for the non-SMGs is 2.43 dex, nearer to the local value of 2.64 dex, the median q_{IR} value among all SMGs in the sample is 2.14 dex, a factor of $\sim$3.2 times lower than the canonical value.

The errors in L_{IR}^{all} appear too small to explain this systematic departure from the canonical IR/radio ratio among the SMGs; by increasing L_{IR}^{all} values by the 3σ errors and recomputing q_{IR}, the median value among the SMGs is 2.16 dex, still a factor for $\sim$3 times lower than the canonical ratio. This result is consistent with the findings of Kovács et al. (2006) who reported similarly low IR/radio ratios for a sample of $\approx$15 SMGs out to $z \sim 3.5$ detected at 350 and 850 μm. The possible reasons for the observed systematic departure off the FIR–radio correlation for this galaxy population are discussed below.

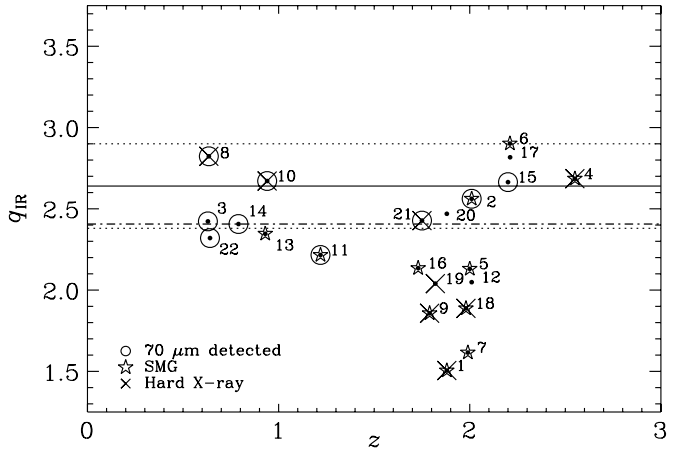

Figure 11. Plot of q_{IR} ratios, as defined in Equation (1), calculated using IR luminosities from SED fitting all available data against redshift. The solid line indicates the local average q_{IR} value of 2.64 (Bell 2003) and the dotted lines are the $\pm 1\sigma$ values. The thick dot–dash line indicates the median value for the sample and falls just above the -1σ line.

5.4. Physical Explanations for Differences in q_{IR} among the SMGs

Assuming that the uncertainty in our estimates of IR luminosity are not responsible for the low IR/radio ratios among the SMGs, there are a number of physical explanations for why galaxies may have IR/radio ratios that are significantly lower than the local correlation value. First we note that a single spectral index was used to *K*-correct all of the observed radio flux densities. While we have assumed a radio spectral index of $\alpha \approx 0.8$, it would take a negative slope (i.e., $\alpha \approx -0.4$) to return the average IR/radio ratio back to the canonical value for the SMGs. Flat or inverted spectra associated with such indices are indicative of AGN (e.g., gigahertz peaked sources arising from synchrotron self-absorption). The radio spectral slopes for $z \sim 2$ ULIRGs are typically not found to exhibit such indices; Sajina et al. (2008) report that only 3/48 *Spitzer*-selected ULIRGs have radio spectral indices between 610 MHz and 1.4 GHz (i.e., $\alpha_{1.4\mathrm{GHz}}^{610\mathrm{MHz}}$) < 0.4. Each of these sources also shows very weak PAH emission which is unlike the SMGs presented here.

Kovács et al. (2006) attributed the low IR/radio ratios to a possible decrease in the effective dust emissivity index for SMGs compared to local star-forming galaxies. However, this is hard to prove without a fine sampling of the full IR SED. The simplest explanation is extra radio emission due to the presence of an AGN. Optical spectroscopy of the SMGs indicates the presence of AGN activity (e.g., Swinbank et al. 2004; Chapman et al. 2005). Analysis of the X-ray data on SMGs also indicates the presence of an AGN in most SMGs (Alexander et al. 2005). Thus, it is very likely that some of the radio emission arises from the nuclear black hole as can be seen by the fact that a number of the most deviant q_{IR} values are in fact detected in the hard band (2.0–8.0 keV) X-rays.

In order to assess if the departure from the canonical q_{IR} value for the SMGs is due to radio emission from an AGN, we recompute q_{IR} ratios by first subtracting the AGN component of the IR luminosity and attempting to make a similar correction to the radio. This is done by assuming that, like the IR emission, the radio emission of Mrk 231 is dominated by its AGN. This is reasonable since Mrk 231 has a $q_{IR} = 2.39$, nearly a factor of $\sim$2 below the nominal value for star-forming galaxies. Taking the 20 cm flux density of Mrk 231 of 0.309 Jy (Condon et al. 2002a) along with its redshift ($z = 0.042$), the corresponding 20 cm specific luminosity is $3.36 \times 10^{-3} L_{\odot}\mathrm{Hz}^{-1}$. The fraction of radio power associated with the AGN for each galaxy was then estimated by scaling the radio luminosity of Mrk 231 by the mid-infrared AGN fractions of the mid-infrared luminosity obtained in Section 3.5. This contribution is then subtracted from the measured 20 cm specific luminosities for each galaxy before computing the new IR/radio ratios.

Rather than decreasing the dispersion among the sample galaxies, this attempt to remove emission arising from the AGN has actually increased the dispersion from 0.49 to 0.54 dex. This result suggests that the fractional infrared output of the AGN does not scale with the fractional output in the radio, consistent with what was found in Section 5.1 by comparing the fractional AGN power with q_{IR}.

Another explanation for the low IR/radio ratios may be related to galaxy–galaxy interactions. The morphology of SMGs seems to suggest major mergers which are driving intense bursts of star formation (e.g., Chapman et al. 2003). In the local universe, a number of interacting galaxy pairs (i.e., so called "Taffy" galaxies) exhibit IR/radio ratios which are a factor of $\sim$2 lower than the canonical value (Condon et al 1993; Condon et al. 2002b). These systems are characterized by a synchrotron "bridge," a region of bright radio continuum connecting the galaxy pairs which is thought to arise from a recent interaction and likely contain both cosmic rays and magnetic fields. The excess radio emission arising from the gaps between these galaxy pairs typically accounts for half of the total radio emission from the entire system. If SMGs have indeed undergone a similar major-merger event, leading to molecular gas and synchrotron bridges between galaxy pairs which do not yet facilitate a significant amount of ongoing star formation, this scenario may explain the lower IR/radio ratios.

On the other hand, perhaps the extreme starbursts occurring within SMGs lead to physical conditions which affect the acceleration and cooling processes of cosmic-ray electrons which boost the synchrotron emissivity. The sample of SMGs presented here is far too small to properly address this question, which will be discussed in a future paper.

5.5. IR and X-Ray Luminosities

A comparison of the AGN and 0.5–8.0 keV luminosities are shown in Figure 12 for the entire sample. There exists a loose relationship between the IR and full band X-ray luminosities of AGN dominated sources (i.e., quasars) such that $L_{0.5-8.0\mathrm{keV}}/L_{\mathrm{IR}} \sim 0.025$ (e.g., Elvis et al. 1994) as indicated by the solid line in Figure 12. We also include the fit to AGN-classified SMGs presented in Alexander et al. (2005) having an average $L_{0.5-8.0\mathrm{keV}}/L_{\mathrm{IR}}$ ratio of $\sim$0.002.

When the AGN luminosities are plotted against the full band X-ray luminosities we find that nearly every galaxy, save GN-IRS 1 and GN-IRS 10, remains either near or above the AGN-classified SMG relation and well away from the canonical AGN relation line for quasars. Despite the fact that GN-IRS 1 and GN-IRS 10 are hard band X-ray detected, they have mid-infrared AGN fractions which are $\lesssim$50%. In fact, the median mid-infrared AGN fraction among all hard band X-ray detected sources is $\sim$44% with a range of $\sim$23%–62%. This indicates that a hard band X-ray detection does not necessarily imply a galaxy is AGN dominated.

We believe that the reason most sources lie generally above the AGN-classified SMG relation is primarily from the

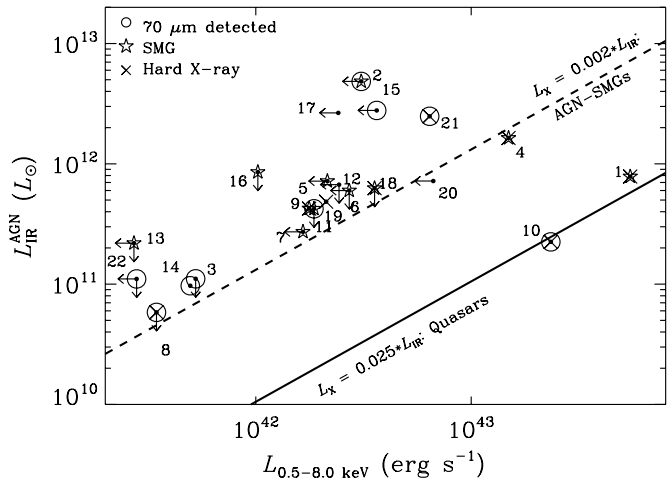

Figure 12. Estimated AGN contribution to the total IR luminosities are plotted against the 0.5–8.0 keV luminosities. Upper limits to the AGN and X-ray luminosities are identified by appropriately directioned arrows. The solid line indicates the canonical relation between the IR and X-ray luminosities of AGN-dominated sources (i.e., quasars) reported by Elvis et al. (1994). The dashed line indicates the fit to AGN-classified SMGs presented in Alexander et al. (2005) and assumes an AGN-IR luminosity fraction of 100%. The three Compton-thick AGN (i.e., GN-IRS 2, 15, and 17) have dust covering fractions significantly larger than that of typical quasars.

overestimation of AGN luminosities; as previously stated, the mid-infrared AGN fractions and associated AGN luminosities should be thought of as upper limits since hot dust contributing to the mid-infrared continuum emission may be powered by star formation. Alternatively, there is some uncertainty on the absorption corrections to the X-ray flux, and it is possible that they could be a factor of ∼2 higher (Alexander et al. 2008b). It is also possible that the AGN in these sources contribute significantly more to the total IR output than the few percent suggested for SMGs by Alexander et al. (2005) arising from a large AGN dust covering factor. The four galaxies having the largest mid-infrared AGN fractions (GN-IRS 2, 15, 17, and 21), three of which are thought to be Compton-thick AGNs (GN-IRS 2, 15, and 17), all lie well away from the typical quasar relation suggesting that they have significantly larger dust covering fractions than quasars.

6. CONCLUSIONS

In the present study, we have used observations from the mid-infrared to the submillimeter to properly characterize the IR luminosities for a diverse sample of 22 galaxies spanning a redshift range of $0.6 \lesssim z \lesssim 2.6$. In addition, we have used the mid-infrared spectra of these sources to estimate the fractions of their IR luminosities which arise from an AGN. Our conclusions can be summarized as follows.

1. IR (8–1000 μm) luminosities derived by SED fitting observed 24 μm flux densities alone are well matched to those when additional mid-infrared spectroscopy and 16, 70, and 850 μm photometry are included in the fits for galaxies having $z \lesssim 1.4$ and L_{IR}^{24} values typically $\lesssim 3 \times 10^{12} L_\odot$. In contrast, for galaxies lying in a redshift range between 1.4 and 2.6 with L_{IR}^{24} values typically $\gtrsim 3 \times 10^{12} L_\odot$, IR luminosities derived by SED template fitting using observed 24 μm flux densities alone overestimate the true IR luminosity by a factor of ∼5, on average, compared to fitting all available data. A comparison between the observed mid-infrared spectra with that of the SEDs chosen from fitting 24 μm photometry alone and from fitting all available photometric data demonstrates that local high luminosity SED templates show weaker PAH emission by an average factor of ∼5 in this redshift range and do not properly characterize the contribution from PAH emission.
2. After decomposing the IR luminosity into star forming and AGN components, we find the AGN luminosity to be increasing with increasing difference between the 24 μm-derived and our best-fit IR luminosities. Such a trend suggests that the AGN power increases with mid-infrared luminosity. However, we also find that the median fraction of the AGN to the difference between the 24-μm-derived and best-fit IR luminosities is only 16% suggesting the AGN power is almost negligible compared to the bolometric correction necessary to properly calibrate the 24-μm-derived IR luminosities.
3. Infrared luminosities calculated using both mid-infrared and 70 μm photometry agree to within ∼50%, on average, to those calculated using additional mid-infrared spectroscopic and submillimeter data and do not show any systematic deviations with increasing redshift. Including the submillimeter photometry in this calculation improves the agreement between the two sets of IR luminosities to within ∼20%. This result implies that IR luminosities derived for deep fields having 70 μm data, like the FIDEL fields, should be able to obtain fairly reliable estimates for the total IR luminosity of sources up to $z \sim 3$ even in the absence of submillimeter data. This will be investigated for GOODS-N in a forthcoming paper.
4. Even after correcting for the presence of an AGN, IR-based SFRs are still larger than those derived from extinction-corrected UV measurements by a factor of ∼2.8, on average, for the $1.4 \lesssim z \lesssim 2.6$ galaxies with secure estimates of their rest-frame UV slopes. Or, in other words, the AGN emission is only able to account for ∼35% of the "excess" IR emission, on average, and is not the dominant cause of the mid-infrared excesses observed in these systems. This suggests that either the SED fitting is overestimating the total IR luminosity, which seems unlikely given the small uncertainties associated with our fitting, or perhaps that the UV extinction correction underestimates the true extinction factors for these galaxies.
5. By using proper bolometric corrections and correcting for the presence of AGN, we are able to account for half of the sources which are identified to have a "mid-infrared excess," as defined by Daddi et al. (2007a), based on their 24-μm-derived IR luminosities. This indicates that the sky and space densities of Compton-thick AGNs reported by Daddi et al. (2007b) are likely high by a factor of ∼2. We therefore report corrected sky density for Compton-thick AGNs of ∼1600 deg^{-2}, and a corresponding space density of $\sim 1.3 \times 10^{-4}$ Mpc^{-3}.
6. We do not see any clear signatures of evolution in the FIR–radio correlation with redshift out to $z \sim 2.6$ for this sample of galaxies. However, the median IR/radio ratio measured for the SMGs included in our IRS-selected subsample is 2.14 dex, a factor of ∼3 lower than what is found locally for star-forming galaxies.
7. A comparison of the estimated AGN and full band (0.5–8.0 keV) X-ray luminosities indicate a higher IR output than observed canonically for quasars for the majority of X-ray-detected sources in the sample. This can be explained

if the AGN luminosities are being overestimated due to star formation contributing significantly to the hot dust continuum in the mid-infrared or if the AGN dust covering factor is large in these sources.

We thank M. T. Huynh and D. Frayer for useful discussions. We also thank the anonymous referee for useful suggestions which helped to improve the paper. D.M.A. acknowledges funding from the Royal Society. This work is based on observations made with the *Spitzer Space Telescope*, which is operated by the Jet Propulsion Laboratory, California Institute of Technology, under a contract with NASA. Support for this work was provided by NASA through an award issued by JPL/Caltech.

REFERENCES

Alexander, D. M., Bauer, F. E., Chapman, S. C., Smail, I., Blain, A. W., Brandt, W. N., & Ivison, R. J. 2005, ApJ, 632, 736
Alexander, D. M., Brandt, W. N., Hornschemeier, A. E., Garmire, G. P., Schneider, D. P., Bauer, F. E., & Griffiths, R. E. 2001, AJ, 122, 2156
Alexander, D. M., et al. 2003, AJ, 126, 539
Alexander, D. M., et al. 2008a, ApJ, 687, 835
Alexander, D. M., et al. 2008b, AJ, 135, 1968
Allamandola, L. J., Tielens, A. G. G. M., & Barker, J. R. 1985, ApJ, 290, L25
Armus, L., et al. 2007, ApJ, 656, 148
Bell, E. F. 2003, ApJ, 586, 794
Borys, C., Chapman, S., Halpern, M., & Scott, D. 2003, MNRAS, 344, 385
Brandl, B. R., et al. 2006, ApJ, 653, 1129
Buat, V., et al. 2007, ApJS, 173, 404
Capak, P., et al. 2004, AJ, 127, 180
Chapman, S. C., Blain, A. W., Smail, I., & Ivison, R. J. 2005, ApJ, 622, 772
Chapman, S. C., Windhorst, R., Odewahn, S., Yan, H., & Conselice, C. 2003, ApJ, 599, 92
Chary, R.-R. 2007, in ASP Conf. Ser. 380, At the Edge of the Universe, ed. J. Afonso, H. Ferguson, & R. Norris (San Francisco, CA: ASP), 375
Chary, R.-R., & Elbaz, D. 2001, ApJ, 556, 562
Cohen, J. G., Cowie, L. L., Hogg, D. W., Songaila, A., Blanford, R., Hu, E. M., & Shopbell, P. 1996, ApJ, 471, L5
Cohen, J. G., Hogg, D. W., Blandford, R., Cowie, L. L., Hu, E., Songaila, A., Shopbell, P., & Richberg, K. 2000, ApJ, 538, 29
Condon, J. J. 1992, ARA&A, 30, 575
Condon, J. J., Anderson, M. L., & Helou, G. 1991, ApJ, 376, 95
Condon, J. J., Cotton, W. D., & Broderick, J. J. 2002a, AJ, 124, 675
Condon, J. J., Helou, G., & Jarrett, T. H. 2002b, AJ, 123, 1881
Condon, J. J., Helou, G., Sanders, D. B., & Soifer, B. T. 1993, AJ, 105, 1730
Cowie, L. L., Barger, A. J., Hu, E. M., Capak, P., & Songaila, A. 2004, AJ, 127, 3137
Daddi, E., et al. 2007a, ApJ, 670, 156
Daddi, E., et al. 2007b, ApJ, 670, 173
Dale, D. A., & Helou, G. 2002, ApJ, 576, 159
Dale, D. A., Helou, G., Contursi, A., Silbermann, N. A., & Kolhatkar, S. 2001, ApJ, 549, 215
Dale, D. A., et al. 2005, ApJ, 633, 857
de Jong, T., Klein, U., Wielebinski, R., & Wunderlich, E. 1985, A&A, 147, L6
Desai, V., et al. 2007, ApJ, 669, 810
Dey, A., et al. 2008, ApJ, 677, 943
Dickinson, M., et al. 2003, in The Mass of Galaxies at Low and High Redshift, ed. R. Bender & A. Renzini (Berlin: Springer), 324
Draine 2003, ApJ, 598, 1017
Dunne, L., Eales, S., Edmunds, M., Ivison, R., Alexander, P., & Clements, D. L. 2000, MNRAS, 315, 115
Elbaz, D., et al. 2002, A&A, 384, 848
Elvis, M., et al. 1994, ApJS, 95, 1
Engelbracht, C. W., et al. 2006, ApJ, 642, L127
Frayer, D. T., et al. 2006, ApJ, 647, L9
Frayer, D. T., et al. 2009, AJ, submitted (arXiv:0902.3273)
Giavalisco, M., et al. 2004, ApJ, 600, L93
Gonzalez, A. H., Clowe, D., Bradac, M., Zaritsky, D., Jones, C., & Markevitch, M. 2009, ApJ, 691, 525
Helou, G., Soifer, B. T., & Rowan-Robinson, M. 1985, ApJ, 298, L7
Huynh, M. T., Pope, A., Frayer, D. T., & Scott, D. 2007, ApJ, 659, 305
Kennicutt, R. C., Jr. 1998, ARA&A, 36, 189
Kovács, A., Chapman, S. C., Dowell, C. D., Blain, A. W., Ivison, R. J., Smail, I., & Phillips, T. G. 2006, ApJ, 650, 592
Lagache, G., Dole, H., & Puget, J.-L. 2003, MNRAS, 338, 555
Le Floc'h, E., et al. 2005, ApJ, 632, 169
Leger, A., & Puget, J. L. 1984, A&A, 137, L5
Madden, S. C., Galliano, F., Jones, A. P., & Sauvage, M. 2006, A&A, 446, 877
Magnelli, B., Elbaz, D., Chary, R. R., Dickinson, M., Le Borgne, D., Frayer, D. T., & Willmer, C. N. A. 2009, A&A, 496, 57
Mainieri, V., et al. 2005, A&A, 437, 805
Meurer, G. R., Heckman, T. M., & Calzetti, D. 1999, ApJ, 521, 64
Murphy, E. J., Helou, G., Kenney, J. D. P., Armus, L., & Braun, R. 2008, ApJ, 678, 828
Murphy, E. J., et al. 2006, ApJ, 638, 157
Owen, F., & Morrison, G. 2008, AJ, 136, 1889
Papovich, C., et al. 2007, ApJ, 668, 45
Pope, A., Borys, C., Scott, D., Conselice, C., Dickinson, M., & Mobasher, B. 2005, MNRAS, 358, 149
Pope, A., et al. 2006, MNRAS, 370, 1185
Pope, et al. 2008a, ApJ, 675, 1171
Pope, et al. 2008b, ApJ, 689, 127
Reddy, N. A., Steidel, C. C., Fadda, D., Yan, L., Pettini, M., Shapley, A. E., Erb, D. K., & Adelberger, K. L. 2006, ApJ, 644, 792
Rigby, J. R., et al. 2008, ApJ, 675, 262
Sajina, A., Yan, L., Armus, L., Choi, P., Fadda, D., Helou, G., & Spoon, H. 2007, ApJ, 664, 713
Sajina, A., et al. 2008, ApJ, 683, 659
Salpeter, E. E. 1955, ApJ, 121, 161
Siana, B., Teplitz, H. I., Chary, R.-R., Colbert, J., & Frayer, D. T. 2008, ApJ, 689, 59
Smith, J. D. T., et al. 2007, ApJ, 656, 770
Steidel, C. C., Hunt, M. P., Shapley, A. E., Adelberger, K. L., Pettini, M., Dickinson, M., & Giavalisco, M. 2002, ApJ, 576, 653
Swinbank, A. M., Smail, I., Chapman, S. C., Blain, A. W., Ivison, R. J., & Keel, W. C. 2004, ApJ, 617, 64
Teplitz, H. I., Charmandaris, V., Chary, R., Colbert, J. W., Armus, L., & Weedman, D. 2005, ApJ, 634, 128
Weingartner, J. C., & Draine, B. T. 2001, ApJ, 548, 609
Wilson, G. W., et al. 2008, MNRAS, 390, 1061
Wirth, G. D., et al. 2004, AJ, 127, 3121
Yun, M. S., Reddy, N. A., & Condon, J. J. 2001, ApJ, 554, 803